Yet another caveat to using the Dessler-Parker-Sckopke relation

M. W. Liemohn

Space Physics Research Laboratory, University of Michigan, Ann Arbor, Michigan, USA

[1]   The analytical formulation of the Dessler-Parker-Sckopke (DPS) equation relating the energy content of the ring current to the magnetic field depression at the Earth's center is examined. To conduct this study, a method is presented for numerically integrating inner magnetospheric pressure distributions according to the Biot-Savart law to obtain magnetic field perturbations at an arbitrary location. It is found that the implicit assumption of the DPS relation requiring that all of the particle pressure is included in the integration can generate large errors relative to the true perturbation. When there is a nonzero pressure just inside the outer boundary of the integration volume, the DPS relation implicitly includes large azimuthal currents at this pressure discontinuity. By including ghost cells of adiabatically decreasing pressure beyond the outer boundary, a "true" perturbation from the currents within the simulation is obtained. The ratio of this corrected value to the DPS value systematically varies according to a simple pressure ratio. Other aspects of the DPS relation are also confirmed with this code, including the validity criterion imposed by the plasma pressure anisotropy and the validity of the relation for any local time asymmetry. The inclusion of closure currents in the perturbation calculation, which were not part of the DPS derivation, changes the local time profile of the perturbation and can make either a negligible or a substantial contribution in either a positive or a negative sense to the globally averaged perturbation.   *INDEX TERMS:* 2778 Magnetospheric Physics: Ring current; 2788 Magnetospheric Physics: Storms and substorms; 2730 Magnetospheric Physics: Magnetosphere—inner; 7819 Space Plasma Physics: Experimental and mathematical techniques; *KEYWORDS:* ring current, storms, magnetic disturbances

1.   Introduction

[2]   *Dessler and Parker* [1959] developed an extremely compact and remarkably useful formula relating the total energy of the ring current E_{RC} to the magnetic field perturbation at the center of the Earth $\Delta B(0)$

$$\frac{\Delta B(0)}{B_E} = -\frac{2E_{RC}}{3U_E}, \quad (1)$$

where B_E is the equatorial surface magnetic field strength of the Earth's dipole and U_E is the magnetic energy of the dipole field beyond the Earth's surface. This equation can be rewritten in standard units in the following form:

$$\Delta B[\text{nT}] = -3.98(10^{-30})*E_{RC}[\text{keV}]. \quad (2)$$

Dessler and Parker's original analysis only considered two particle distributions, isotropic and completely equatorial, but *Sckopke* [1966] extended the validity of this formulation for all pitch angle distributions of the form $\sin^{\gamma}\alpha$, where α is

the equatorial pitch angle and $\gamma \geq 0$. Equation (1) (and equation (2)) is now known as the Dessler-Parker-Sckopke (DPS) relation and has been used extensively in geomagnetic storm analyses to understand the *Dst* index and to parameterize the overall strength of the ring current [see, e.g., *Roeder et al.*, 1996; *Jorgensen et al.*, 1997; *Greenspan and Hamilton*, 2000]. Large-scale ring current modeling has shown that this formula can reproduce the observed *Dst** (the ring current contribution to the *Dst* index, often treated as equivalent to $\Delta B(0)$) to within 20% during most storms [e.g., *Jordanova et al.*, 1998, 2001; *Ebihara and Ejiri*, 1998; *Kozyra et al.*, 1998, 2002; *Liemohn et al.*, 1999, 2001a]. Differences between the observed and predicted *Dst** values have normally been attributed to the simulation boundary conditions or background magnetic and electric field choices. Because of its simplicity and relative accuracy, it remains one of the most used formulas in ring current analyses.

[3]   Problems and inadequacies in this relation have not gone unnoticed, however. These studies do not disprove the derivation of the DPS relation so much as quantify the errors introduced in the analytical assumptions used by *Dessler and Parker* [1959] and *Sckopke* [1966]. For instance, *Carovillano and Siscoe* [1973] presented a detailed analysis of the early studies examining and aug-

menting the DPS relation. These include the omission of a nonlinear energy term in the original derivation [*Parker and Stewart*, 1967; *Baker and Hurley*, 1967; *Maguire and Carovillano*, 1968]. This term was omitted because *Dessler and Parker* [1959] assumed linear field distortions and did not take into account effects of the field perturbation on the motion of the particles creating the magnetic field depression. This feedback is a natural consequence seen in the virial theorem, which equates changes to the total magneto-hdrodynamic energy in a volume to the energy flow through its boundary surface. Estimations of the magnitude of this nonlinear term reveal that the DPS relation has up to a 30% underestimation of the true magnetic field perturbation [*Hoffman and Bracken*, 1967; *Sozou and Windle*, 1969a, 1969b; *Lackner*, 1970].

[4] Another assumption is azimuthal (local time) symmetry of the magnetospheric pressures and currents. *Carovillano and Siscoe* [1973], however, showed that the DPS relation is actually valid for asymmetric currents; it just takes into account only the perpendicular magnetospheric currents and neglects the perturbation from the field-aligned and ionospheric closure currents. If one assumes that the field-aligned current contribution is masked by the ionospheric Pedersen current contribution to the perturbation, as is done for deconvolving high-latitude magnetometer data [e.g., *Ahn et al.*, 1983], then the DPS relation is valid for any current configuration in the inner magnetosphere.

[5] More recently, *Siscoe and Petschek* [1997] and *McPherron* [1997] examined the validity of the DPS relation and found that another term, the net inflow of particle energy into the volume, must also be included in the calculation of the field depression. This term accounts for the dynamics of the stormtime ring current, being largely responsible for the growth and decay of the total particle energy and thus the magnetic perturbation. *Siscoe and Petschek* [1997] showed that during substorms, most of the magnetic energy released during dipolarization is deposited directly into the ionosphere (Joule heating and precipitative power) rather than transferred into magnetospheric particle energy. This results in a recovery in addition to any substorm current wedge influences on *Dst*, which are also positive [*Friedrich et al.*, 1999; *Munsami*, 2000]. It should be noted, however, that while *Dst* and *AL* have been correlated [*Davis and Parthasarathy*, 1967; *Cade et al.*, 1995], others have found that the source of the ring current energy cannot be substorms [*McPherron*, 1997; *Wolf et al.*, 1997; *Grafe*, 1999, *Fok et al.*, 1999; *Grafe and Feldstein*, 2000; *Liemohn and Kozyra*, 2002].

[6] The present study examines yet another difference between reality and the assumptions used in obtaining the DPS relation. Specifically, the impact of a nonzero pressure at the outer boundary of the integration volume is investigated. Details are presented of a method for calculating the magnetic field depression generated by energetic particles in the inner magnetosphere. This formulation is derived and presented for an arbitrary location of the "virtual magnetometer." Comparisons are made between ΔB from the DPS relation and ΔB at virtual magnetometers placed at several locations. It is concluded that the DPS formulation overpredicts the perturbation from the inner magnetospheric currents because of the truncation error associated with a nonzero pressure just inside the outer boundary. The ramifications of this adjustment to our understanding of the DPS relation are discussed in section 5.

2. Numerical Solution of the Biot-Savart Integral

[7] As is known from classic electrodynamics, a line of current generates a cylindrical magnetic field around it. The formal equation relating these two quantities is known as the Biot-Savart law, which gives the resulting magnetic field vector $\Delta \mathbf{B}$ at an arbitrary location $\mathbf{r}$ from a vector current density field $\mathbf{J}(\mathbf{r}')$ distributed throughout a volume V

$$\Delta \mathbf{B}(\mathbf{r}) = \frac{\mu_0}{4\pi} \int_V \frac{\mathbf{J}(\mathbf{r}') \times (\mathbf{r} - \mathbf{r}')}{|\mathbf{r} - \mathbf{r}'|^3} d\mathbf{r}', \quad (3)$$

where μ_0 is the permeability of free space. The current density in the inner magnetosphere can be easily derived from the hot particle pressures [e.g., *Parker*, 1957]

$$\mathbf{J}_\perp = \frac{\mathbf{B}_0}{B_0^2} \times \left[\nabla P_\perp + \left(P_\parallel - P_\perp \right) \frac{\nabla B_0}{B_0} \right], \quad (4)$$

where $\mathbf{B}_0$ and B_0 are the vector and total magnitude quantities of the background magnetic field, respectively. For this study the numerical method of *Liemohn et al.* [2001b] will be used to determine the perpendicular currents in the magnetosphere $\mathbf{J}_\perp$. Note that there is both a "radial" and an "azimuthal" component to $\mathbf{J}_\perp$ (both orthogonal to the local field line direction, so the radial component is actually directed straight outward only at the equator). The particle pressures in equation (4) are found from the moments of the local plasma distribution function f

$$P_\perp = \pi \int f(v, \alpha) m v^2 \sin^3 \alpha \, dv \, d\alpha$$
$$P_\parallel = 2\pi \int f(v, \alpha) m v^2 \cos^2 \alpha \sin \alpha \, dv \, d\alpha, \quad (5)$$

where v and α are the particle velocity and local pitch angle and m is the particle mass. Again, the numerical approach described by *Liemohn et al.* [2001b] will be employed. Because the bounce period of hot ions and electrons is fast compared to their drift and collisional timescales, it is a valid approximation to assume that f at an arbitrary point in space can be found by mapping the distribution at the equatorial plane ("*eq*" subscript) along the field line, changing α according to the first adiabatic invariant

$$\frac{\sin^2 \alpha}{B_0} = \frac{\sin^2 \alpha_{eq}}{B_{0,eq}}. \quad (6)$$

[8] *Liemohn et al.* [2001b] discussed the calculation of field-aligned currents from the divergence of equation (4). The perturbation arising from this component of the current (as well as from the ionospheric currents that must exist to close the field-aligned currents) is included in Appendix A. Only a small portion of the results presented below will include the closure currents, however. The reason for this is that a detailed description of the ionospheric conductances

is needed for a proper definition of the ionospheric currents, and this is beyond the scope of the parametric case studies to be presented. Because these currents can be close to the usual placement of the virtual magnetometers (on the Earth's surface or at the origin), incorrect placement of these currents can result in significant errors in $\Delta\mathbf{B}$. For instance, under the assumptions of a vertical field line and uniform conductance the ionospheric Pedersen currents will have a signal that exactly cancels that from the field-aligned currents, and only the ionospheric Hall currents need to be considered [e.g., *Roble and Ridley*, 1987]. If an electrojet is assumed, then the influence can be tens of nanoteslas [e.g., *Siscoe and Crooker*, 1974]. In addition, high-latitude field-aligned currents can cancel the lower-latitude currents emanating from the integration volume [e.g., *Crooker and Siscoe*, 1981], and so the domain must expand to include all relevant currents that might contribute to the perturbation. This influence is especially strong when examining the local time asymmetries of the magnetic perturbation. Therefore the results below will focus almost entirely on the magnetospheric perpendicular currents and their resulting perturbation. To minimize the effect of this calculational omission, most of the results will be for a symmetric current distribution in azimuth. Longitudinally asymmetric currents will only be shown in section 4.3, along with the influence of the closure currents on the magnetic perturbation.

[9] The numerical algorithm and relevant equations of the integration method are presented in Appendix A, and so only an overview of the general calculational flow scheme is given here. The calculation begins with the definition of a distribution function f in the equatorial plane. This is mapped along the field line using Liouville's theorem to obtain a three-dimensional (3-D) distribution of parallel and perpendicular pressures. Then, equation (4) is used to convert these pressures into currents, and finally equation (3) is used to extract a magnetic perturbation. In addition to calculating $\Delta\mathbf{B}$ from equation (3), a numerical integration of the total energy content of the plasma (from the 3-D particle distribution) is used to obtain a value for E_{RC}. This can then be used in equation (2) to get a DPS perturbation value for comparison. Note that a dipole magnetic field is used throughout this calculation for consistency with the derivation of the DPS relation.

[10] The largest obstacle in solving equation (3) is that the natural coordinates for this calculation are the dipolar unit vectors, because it is convenient to define a particle distribution in the equatorial plane and then map it along the field lines throughout the volume. This system, though, is quite inconvenient for taking cross products and vector subtractions (as is necessary). In the following presentation (as well as in Appendix A) the indices of i, j, and k will be used to denote integration grid cells in the r, φ, and λ directions in dipolar space, respectively. Note that λ is not invariant latitude, but rather the actual latitude of the grid location (along a field line). All vectors, however, are presented in x, y, and z Cartesian coordinates, including the pressure gradients. Therefore the method includes a lengthy routine to calculate the angles and interpolation coefficients for the various derivatives (see Appendix A).

[11] It should be noted that there is a limitation to the validity of this approach. Specifically, all of the numerical grid cell increments should be small compared to both the $|\mathbf{r}'\text{-}\mathbf{r}|$ distance and, to a lesser degree, to the pressure and magnetic field gradients. This is because it is assumed that the entire grid cell is considered to be at a point at the center of the cell. If $|\mathbf{r}'\text{-}\mathbf{r}|$ is comparable to the grid spacing, then the perturbation at $\mathbf{r}$ will greatly depend on its position relative to the nearest grid cell centers. Similarly, if the gradient quantities are large across the grid cell spacing, currents may be incorrectly placed within the volume, leading to errors. This second source of error grows in significance as the first source of error becomes an issue (that is, close to the virtual magnetometers). Both of these limitations can be presumably overcome by reducing the grid spacing (or subgridding).

3. Energetic Particle Distribution Mappings

[12] The topic of collisionless mapping of distributions along field lines (i.e., application of the Liouville theorem) has a long and rich history. Studies have focused on a variety of issues regarding this mapping, on the formation of electrostatic potential differences along a field line [e.g., *Alfvén and Fälthammar*, 1963; *Whipple*, 1977; *Chiu and Schulz*, 1978; *Miller and Khazanov*, 1993], the current-voltage relationship [e.g., *Knight*, 1973; *Stasiewicz*, 1985], or ionospheric outflow quantification [e.g., *Lemaire and Scherer*, 1973, 1974; *Khazanov et al.*, 1997; *Wilson et al.*, 1997; *Su et al.*, 1998]. All of these applications use the same general approach in that they assume a particle distribution function at a reference point along the field line and then collisionlessly map it through the changing B field strength and changing potential energy amplitude. In the discussion below (and in Appendix B), quantities at the reference point along the field line are denoted by the subscript "r."

[13] For the present study it is assumed that the magnetic field lines are equipotentials and that the plasma can be described by a bi-Maxwellian distribution function at the equatorial plane (the chosen reference point). The details of the derivation of the pressures are given in Appendix B, and only the final solutions are shown here. The method of *Liemohn and Khazanov* [1998] was used to determine the pressures, but because of the assumptions listed above, the other approaches should yield exactly the same formulas. The parallel and perpendicular pressures at any point along a field line is expressed in terms of the equatorial plane pressures, $P_{\|r}$ and $P_{\perp r}$, and the magnetic field ratio $R_B = B_r/B$ and have the form

$$P_{\|} = P_{\|r}\frac{A+1}{1+AR_B} \tag{7a}$$

$$P_{\perp} = \frac{P_{\|}}{1+AR_B} = P_{\|r}\frac{A+1}{(1+AR_B)^2}, \tag{7b}$$

where $A = P_{\|r}/P_{\perp r} - 1$. Because the bounce period of typical ring current ions is fast compared to their collisional and drift timescales, the pitch angles that are magnetically connected to the ionosphere are quickly depleted of particles. Analytical formulas for the pressures under an empty loss cone assumption require another magnetic field ratio $R_{BI} = B_I/B$, relating the field strength at the ionospheric
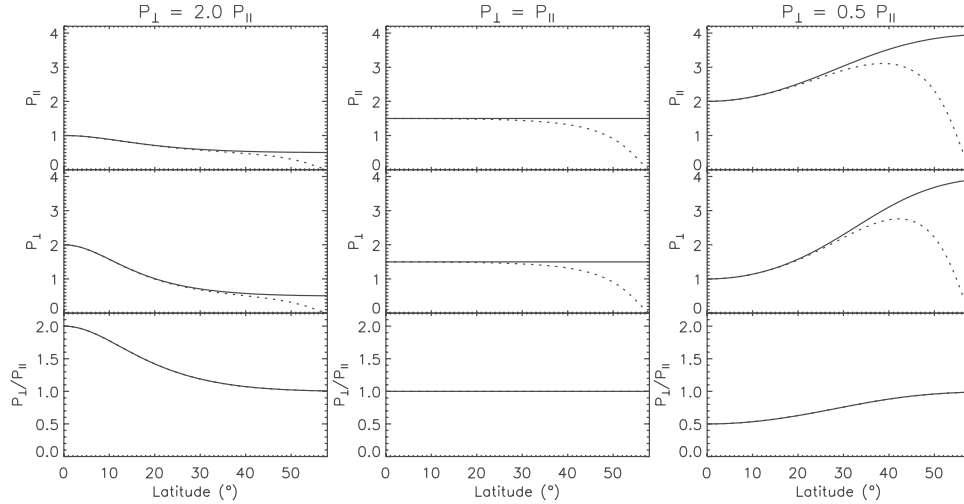
Figure 1. (top) Parallel and (middle) perpendicular pressure distributions and (bottom) their ratio along an $L = 4$ field line for three different anisotropy values. The left panel shows profiles for a pancake distribution, the middle panel shows profiles for an isotropic distribution, and the right panel shows profiles for a cigar distribution. The solid lines are for filled loss cone distributions, while the dotted lines are for empty loss cone distributions.

endpoint (denoted by subscript "I") to the local field strength. The pressures then have the form

$$P_\parallel = P_{\parallel r}^* \frac{A^* + 1}{1 + A^* R_B} \left[\frac{R_{BI} - 1}{R_{BI} - R_B} \right]^{1/2} \left(1 - \frac{1 + A^* R_B}{R_{BI} + A^* R_B} \right) \quad (8a)$$

$$P_\perp = \frac{P_\parallel}{1 + A^* R_B} = P_{\parallel r}^* \frac{A^* + 1}{(1 + A^* R_B)^2} \left[\frac{R_{BI} - 1}{R_{BI} - R_B} \right]^{1/2} \\ \cdot \left(1 - \frac{1 + A^* R_B}{R_{BI} + A^* R_B} \right), \quad (8b)$$

where $A^* = P_{\parallel r}^*/P_{\perp r}^* - 1$. Because of the presence of an empty loss cone, the reference values are slightly modified to recover the original reference values at the equatorial plane

$$P_{\parallel r}^* = P_{\parallel r} \left(1 - \frac{R_B + A R_B}{R_{BI} + A R_B} \right) \quad (9a)$$

$$P_{\perp r}^* = P_{\perp r} \left(1 - \frac{R_B + A R_B}{R_{BI} + A R_B} \right). \quad (9b)$$

For the present study the ionospheric endpoint is taken at 120 km above the Earth's surface.

[14] Figure 1 shows some examples of pressure distributions along a field line. The pressure values are normalized to arbitrary units, and a McIlwain L parameter $L = 4$ dipolar field line is chosen (as a good midpoint of the typical ring current L range). The three panels of Figure 1 show the pressure profiles assuming different anisotropies: $A < 0$ in the left panel (pancake distribution), $A = 0$ in the middle panel (isotropic distribution), and $A > 0$ in the right panel

(cigar distribution). For the filled loss cone distribution (solid lines) it can be seen that the pressures decrease for all latitudes when $A < 0$, are constant with latitude for $A = 0$, and increase with latitude for $A > 0$. Because the higher-pitch angle particles are removed by the mirror force as the magnetic field strength increases along the field line, the low-pitch angle part of f dominates the pressure values at higher latitudes. For the empty loss cone distribution (dotted lines), the pressure drops to zero at the ionospheric endpoint of the field line. The two distributions are quite similar for most of the field line, and it is only near the endpoint that they diverge.

[15] Results using only one of these distributions will be chosen for the remainder of the analysis. The numerically easier choice is the filled loss cone distribution, but the more intuitively correct choice is the empty loss cone distribution. Because we are assuming that the distributions change slowly enough to validate a collisionless mapping along the field line, it makes sense that the loss cone should be depleted. Figure 2 is a quantitative comparison of these two distributions against a simulated distribution from the kinetic drift-loss modeling results of *Kozyra et al.* [2002]. Shown in Figure 2 are comparisons for three times during the magnetic storm of 4–6 1991, with the left panel taken from the main phase, the middle panel taken from the early recovery phase, and the right panel taken from the late recovery phase. For all three of these times the distribution is taken from the location $L = 4$ at magnetic local time (MLT) = 2100, which is near the peak in the simulation results during the main phase. The equatorial perpendicular and parallel pressures are set equal to the simulation result values, and then the two collisionless mapping profiles are shown along with the result from equation (5) using the local velocity space distribution from the simulation results. It is seen that the empty loss cone mapping is much closer to the results from the drift-loss model for all three cases. Therefore the empty loss cone
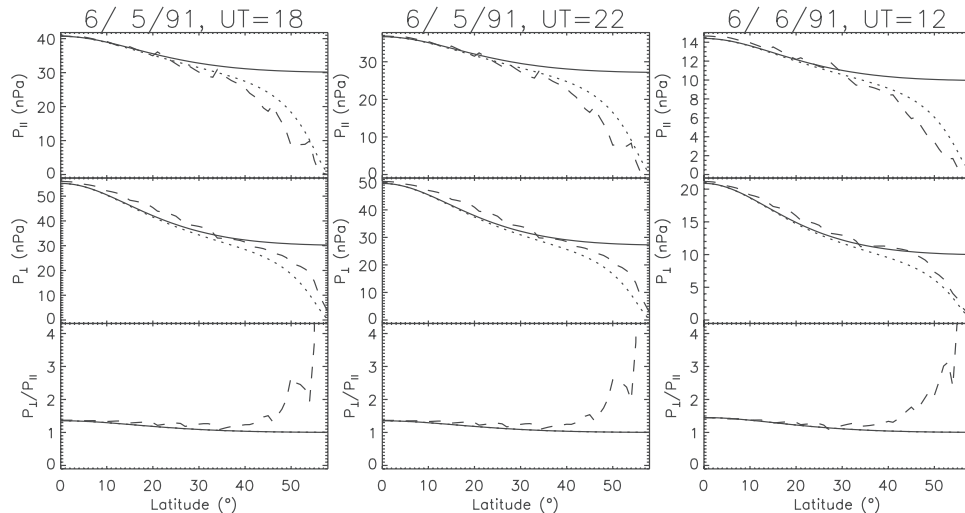
Figure 2. (top) Parallel and (middle) perpendicular pressure distributions and (bottom) their ratio along an $L = 4$ field line at magnetic local time (MLT) = 2100 for three times during a magnetic storm. The main phase is given in the left panel, the peak of the storm is given in the middle panel, and a time well into the recovery phase is given in the right panel. The dashed lines are field line profiles from a kinetic drift-loss model of hot ion transport in the inner magnetosphere, while the solid lines and dotted lines are filled and empty loss cone profiles using the equatorial values of these simulated distributions.

distribution will be used in the following section. Using the filled loss cone distribution will, of course, slightly change the numbers in the plots below, but the main conclusion is unaffected.

4. Comparisons of ΔB Calculations

[16] Using an equatorial plane pressure distribution, the current density throughout the inner magnetosphere can be determined and, using equation (3), the magnetic perturbation at any location can then be calculated. While any definition of $P_\parallel$ and $P_\perp$ in the inner magnetosphere can be used with this technique (that is, extracted from remotely sensed or in situ observations, first-principles models, or empirical descriptions), the following analysis will use an analytically defined pressure distribution. This allows for a better understanding of the comparisons to be made, and the reasons for discrepancies between the methods can be more readily understood.

4.1. Test Calculations

[17] A series of parametric tests have been conducted to determine the accuracy and validity of the method described in sections 2 and 3. Presented here are descriptive highlights of those calculations.

[18] It is useful to quantify the error in the calculation as a function of the plasma pressure distribution. One battery of tests was run with thin shells of plasma around the Earth, essentially a delta function in L shell with azimuthal (local time) symmetry. Figure 3 shows the results of such a calculation for a shell at $L = 4$. The pressure distribution is isotropic with an empty loss cone. The Figures 3a–3d show the equatorial plane pressure distribution, the pressure distribution in the x-z plane, the azimuthal currents resulting from the pressure gradients

using equation (4), and the contribution to ΔB at the center of the Earth from those currents. Note that Figures 3a–3d are normalized to their maximum values (as in all similar plots to follow). It is seen in Figure 3 that the pressures are correctly mapped, the azimuthal currents are correctly determined, and that the contributions to the perturbation are correctly calculated. Westward currents appear on the outer edge of the shell and eastward currents on the inner edge, with corresponding negative and positive contributions to ΔB. Note that the contours in Figure 3d appear to be more confined toward the equator than the contours in Figure 3c. This is because of the geometrical preference of equatorial currents in producing axially aligned perturbations. The magnetic perturbation at Earth's center from this shell is -1.58. The total energy in this thin shell can also be calculated, yielding another perturbation estimate from the DPS relation (equation (2)), which is -1.69. The ratio of the ΔB_{BSI} value to the ΔB_{DPS} value is 0.934 for this location and specification of a thin shell. *Ebihara and Ejiri* [2000, 2001] also found similarity between the perturbation from the DPS relation and that from a Biot-Savart integration of their model results.

[19] To understand if this ratio is particularly good or bad, the shell was moved to many L shells. The resulting $\Delta B_{\mathrm{BSI}}/\Delta B_{\mathrm{DPS}}$ ratios are given in Figure 4. It is seen that the ratio drops from 1.04 at $L = 2$ to 0.92 at $L = 6.5$, with most of the decrease occurring at low L values. A change to a different pressure anisotropy value changes the offset of this line but not the shape. Specifically, it shifts upward for $P_\perp > P_\parallel$ and downward for $P_\parallel > P_\perp$. The difference between this ratio and unity is therefore a systematic error introduced in one or both of the different approaches. It is not a numerical integration error, because increasing the grid resolution (doubling and even tripling
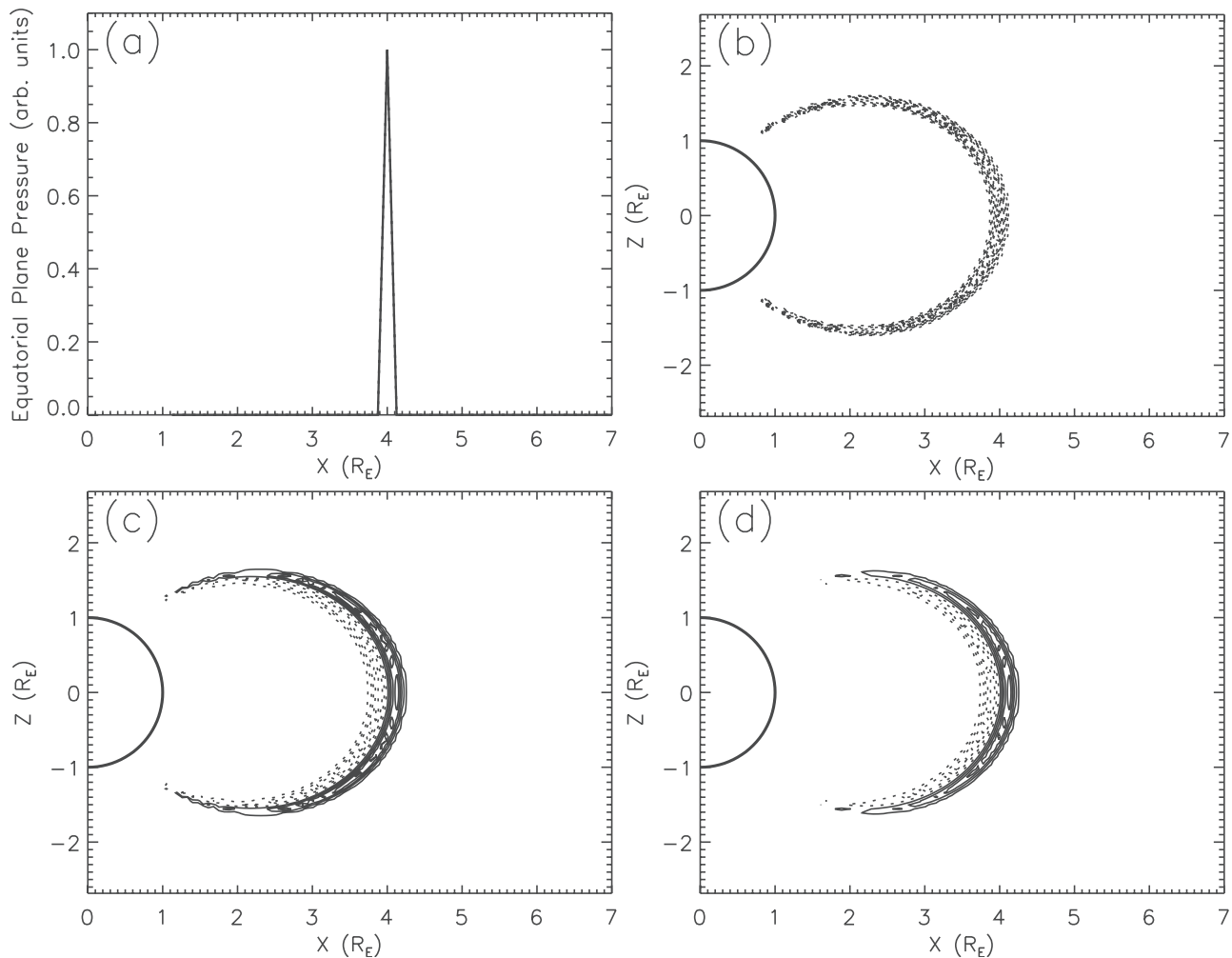
Figure 3. (a) Equatorial plane pressure distribution for a thin shell distribution at $L = 4$, (b) perpendicular pressure distribution in the x-z plane assuming an isotropic distribution with an empty loss cone, (c) azimuthal current distribution in the x-z plane, (d) relative contribution to the north-south magnetic perturbation at the origin ($x = 0$, $z = 0$). Contours are drawn at 0.2 intervals, from -1.0 to 1.0, with dotted contours for negative values and solid contours for positive values. No contour is drawn at 0.0.

the number of cells in each spatial coordinate) has no effect on these ratios (meaning the chosen resolution is sufficient). This systematic error will be discussed in more detail in section 4.3.

[20] Other plasma pressure distributions were also used for testing the algorithm. Figure 5 shows results for an azimuthally symmetric "thick shell" of plasma, with a constant isotropic pressure inside the shell. As expected, the eastward and westward currents are confined to the inner and outer edges of the shell, respectively, with corresponding ΔB contributions. For this distribution, $\Delta B_{\mathrm{BSI}}/\Delta B_{\mathrm{DPS}} = 0.932$. Because the shell is centered at $L = 4$, this value is amazingly close to the thin shell values for this L shell. Changing the location and thickness of the shell results in similar ratios to the thin shell analysis L shell dependence.

[21] As a final presentation of a test case distribution, Figure 6 shows results from a parabolic equatorial pressure variation with L shell, again centered at $L = 4$ with $P_{\parallel} = P_{\perp}$. It is seen that the currents and ΔB contributions are located as expected with reasonable magnitudes. The resulting ΔB

ratio is 0.932, exactly the same as the uniform pressure results. As with the thick shell ΔB values, the ΔB from the parabolic pressure variation also changes like the thin shell results as the location and spread of the distribution is
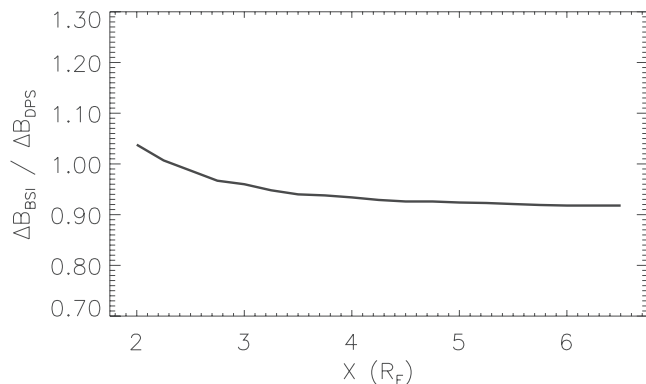

Figure 4. The ratio of ΔB_{BSI} to ΔB_{DPS} for isotropic thin shell distributions as a function of shell location.
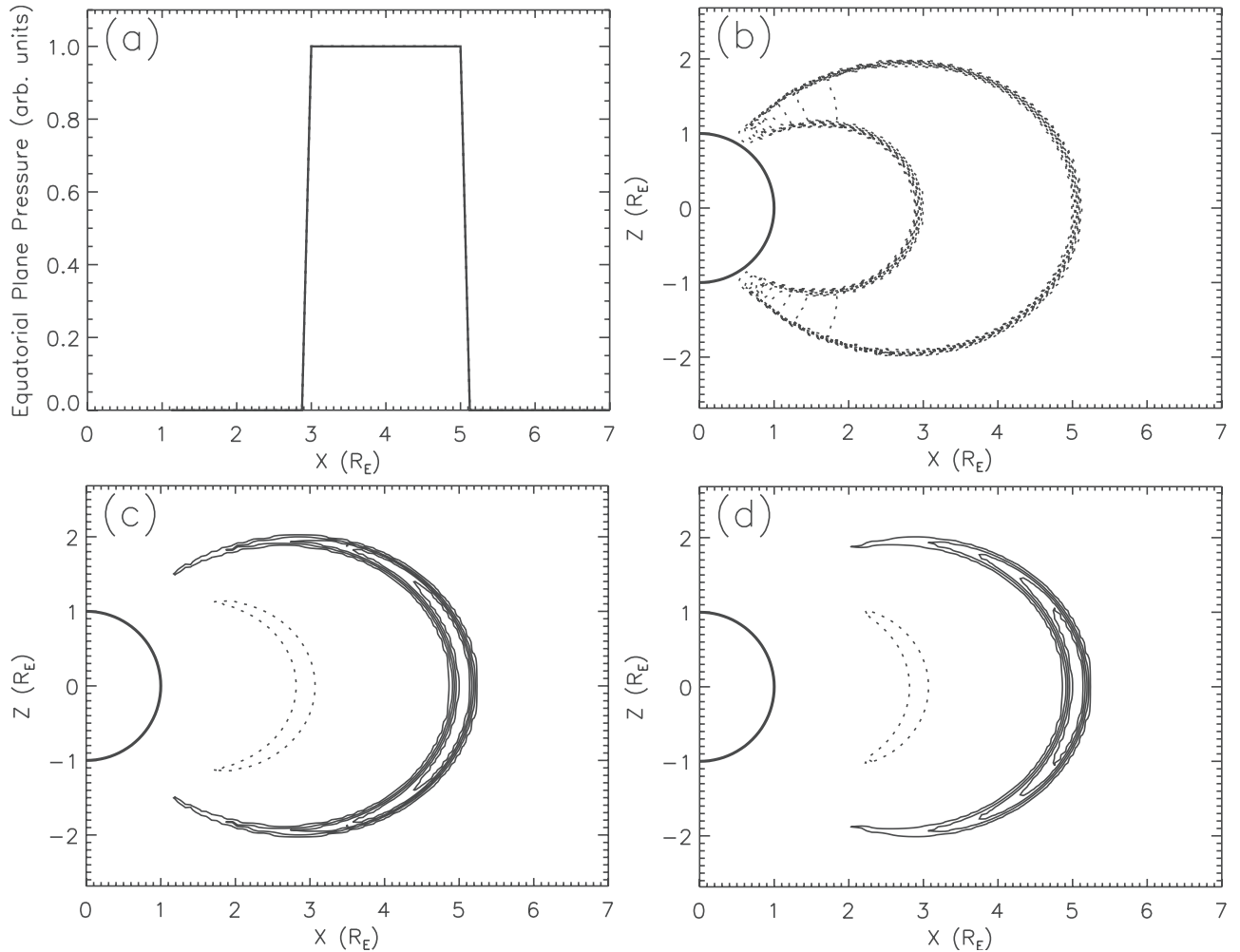
Figure 5. Same four panels as in Figure 3, but for an isotropic thick shell distribution centered at $L = 4$ with a 2 R_E width at the equator.

changed. Other distributions were also applied with similar results.

4.2. Examination of the Truncation Current

[22] In applying the method to real plasma distributions in the inner magnetosphere, it is useful to reduce these distributions to analytical forms. This will provide ease of interpretation of the results without a loss of generality. In examining pressure profiles from in situ satellite data [e.g., *Lui et al.*, 1987, 1994; *Lui and Hamilton*, 1992; *Sheldon and Hamilton*, 1993; *Greenspan and Hamilton*, 2000; *Pulkkinen et al.*, 2001] and model results [e.g., *Chen et al.*, 1994, 2000; *Liemohn et al.*, 2001a], a particular functional form arises as a good fit to the L shell profile of the pressure

$$P_{\parallel,\perp} = x\exp\left[-\frac{x - L_{\mathrm{peak}}}{\Delta L}\right]$$

for   (10)

$$L > L_{\min} = L_{\mathrm{peak}} - \Delta L,$$

where $x = L - L_{\min}$. The parameters L_{peak} and ΔL vary depending on local time, activity level, and storm phase, but the overall functional form appears to be a decently robust fit. As a nominal case, values of $L_{\mathrm{peak}} = 4$ and $\Delta L = 0.625$ will be chosen.

[23] Figure 7 shows the resulting currents and ΔB contributions from this distribution. Note that because the DPS relation assumes inclusion of all plasma pressure within the integration volume V, the pressure is truncated beyond $L = 6.5$ to zero. As can be seen in Figure 7, this truncation results in a massive westward current density at $L = 6.5$ and a correspondingly large ΔB contribution. While such a current system is unrealistic, the resulting ΔB_{BSI} to ΔB_{DPS} ratio is 0.926. The closeness of this number to all the test calculations (which were also peaked/centered at $L = 4$) indicates that this "truncation current" at the boundary is implicitly included in the DPS relation. That is, when equation (2) is used to determine the magnetic perturbation from an inner magnetospheric plasma distribution that does not reach zero, the DPS relation imposes this pressure constraint and thus inserts and integrates over this truncation current.

[24] This should not be a surprising result, because the original derivations by *Dessler and Parker* [1959] and *Sckopke* [1966] analytically solved equation (3) for an infinitesimally small volume element. That is, they included
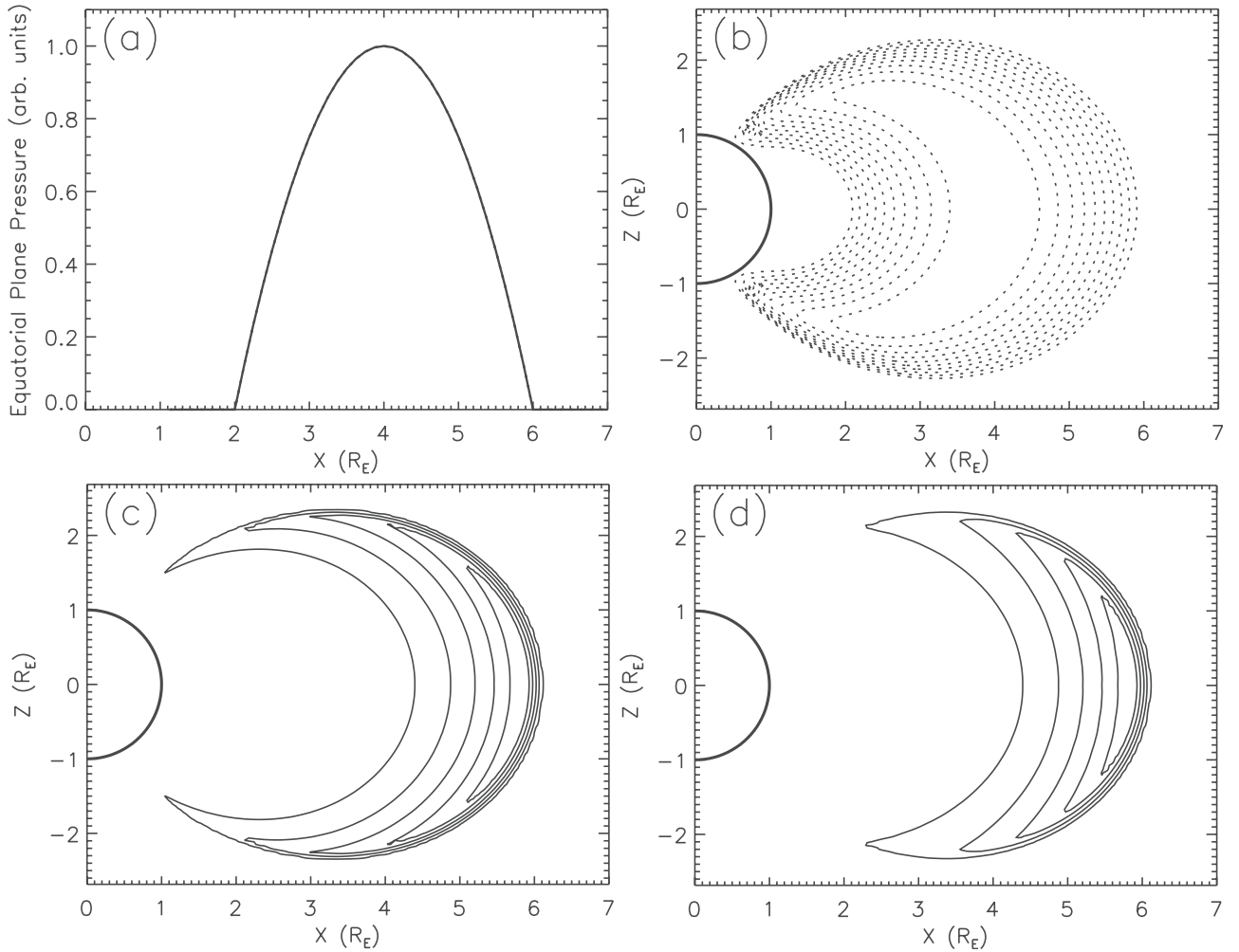
Figure 6.   Same four panels as in Figure 3, but for an isotropic pressure distribution with a parabolic L shell dependence, centered at $L = 4$ with a 4 R_E width at the equator.

in the solution the eastward and westward currents at the inner and outer edges of these volume elements. The neighboring cells, however, cancel some or all of these currents, yielding the correct total perturbation results. So the DPS relation is linearly additive, and any volume integration is equivalent to the sum of N integrations over the N parts of the total volume. At the inner boundary the chosen pressure profile goes to zero, because the plasma stops in the upper atmosphere (and well before that in the equatorial plane). At the outer boundary, often taken at or near geosynchronous orbit in studies of the inner magneto-sphere, the pressure is never zero. So this truncation current is always present.

[25] By the inclusion of ghost cells with nonzero pressure beyond the simulation domain, the truncation current can be removed from the Biot-Savart integration. The outcome of this exercise is shown in Figure 8. The resulting $\Delta B_{\mathrm{BSI}}/\Delta B_{\mathrm{DPS}}$ ratio is 0.700, substantially less than the ratio with the truncation current included. To better understand the quantitative reduction of the perturbation (and to remove the systematic difference between the Biot-Savart integral (BSI) and DPS results), it is useful to consider the ratio of ΔB_{BSI} with the ghost cells included to ΔB_{BSI} without them. This

ratio B_r is 0.755 for this case. This means that 25% of the DPS value is caused by the truncation current. Because this is a nonphysical current which should not have been included in the integration, the DPS relation is always systematically overestimating the perturbation from inner magnetospheric plasma.

[26] Figures 7 and 8 show results for the nominal pressure distribution. The free parameters of L_{peak} and ΔL can be varied to investigate the magnitude of this overprediction by the DPS relation (that is, the contribution from the boundary current). In the course of systematically varying these parameters, an interesting result becomes evident. For a given L_{peak}, as ΔL is increased, the ratio B_r drops. For the same ΔL, as L_{peak} is increased, this ratio drops. Upon a more careful examination of the results, it becomes clear that there is a governing relationship of the variation in this ΔB ratio. The independent variable is the ratio of the peak pressure to the boundary pressure (in this case, the pressure at $L = 6.5$). Figure 9 shows the relationship of B_r to this pressure ratio P_r for an isotropic and a pancake pressure distribution. Eighteen points are shown in Figures 9a and 9b: six values of ΔL for each of three values of L_{peak}. The correlation is remarkable with a precise one-to-one relation-
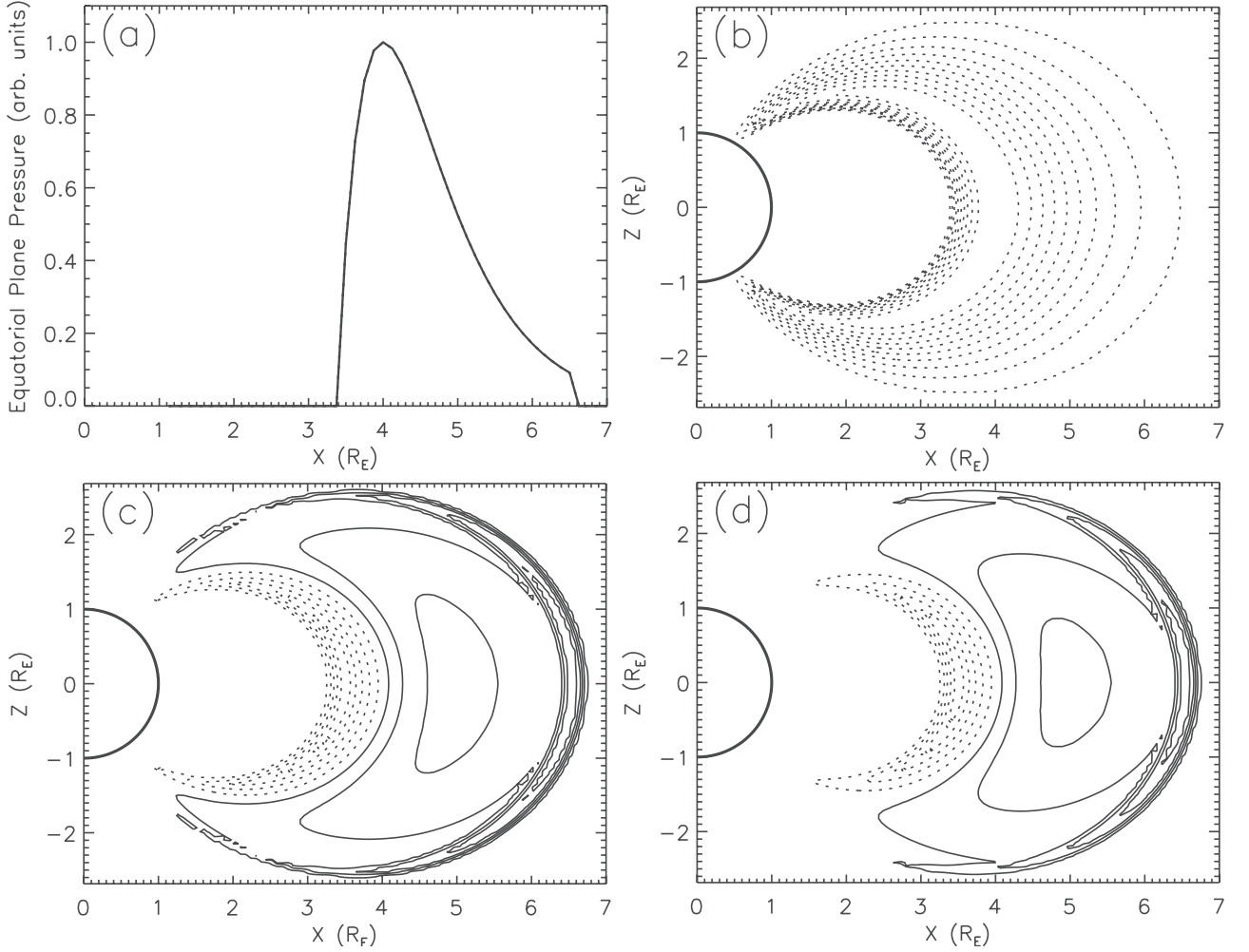
Figure 7. Same four panels as in Figure 3, but for an isotropic pressure distribution with a real L shell dependence, with a truncated pressure at the outer boundary of the integration volume.

ship between the ΔB ratio and the pressure ratio. A line can be fitted through these points which has a functional form of

$$B_r = A - \left[\frac{P_r - B}{C}\right]^D \qquad (11)$$

The four free parameters (A, B, C, and D) are fitted through an iteration routine that randomly changes the values by up to 1% per iteration, seeking to minimize the error between the curve and the points by reducing the following deviation parameter:

$$\delta = \sqrt{\frac{1}{N-1}\sum_{i=1}^{N}\left[B_r^{\text{fit}}(i) - B_r(i)\right]^2}. \qquad (12)$$

Several disparate initial condition sets for A, B, C, and D were used to ensure that a global minimum of δ is found. For the isotropic pressure results (Figure 9a) the best fit coefficients are $A = 0.9914$, $B = 18.80$, $C = 18.57$, and $D = 11.52$, while for the pancake pressure results (Figure 9b) the best fit values are $A = 0.9896$, $B = 18.49$, $C = 18.07$, and

$D = 11.35$. These two sets of values are very similar, with the main difference being a slight downward shift for the pancake pressure results (i.e., a larger influence of the truncation current in the DPS relation). This downward shift is understandable because the pancake distribution confines the currents near the equatorial plane, where they will contribute most to the axial magnetic perturbation at the origin.

[27] In understanding the significance of Figure 9 it is useful to make note of some critical values in the fitted relationships. Table 1 lists some of these numbers for the two cases shown in Figure 9, including the pressure ratios where the magnetic field ratio is 0.0, 0.5, and 0.9. It is interesting that neither fit passes through the origin but rather the magnetic field ratio reaches zero when the pressure ratio is still above unity. This is, of course, an extrapolation of the calculated results, but it demonstrates that the DPS relation profoundly breaks down as the truncation current increases into becoming the dominant contributor to ΔB. Another revelation of Figure 9 and Table 1 is that a pressure ratio of more than 40 is needed for the truncation current to contribute <10% to the ΔB value. Another quantity listed in Table 1 is the B_r value for a
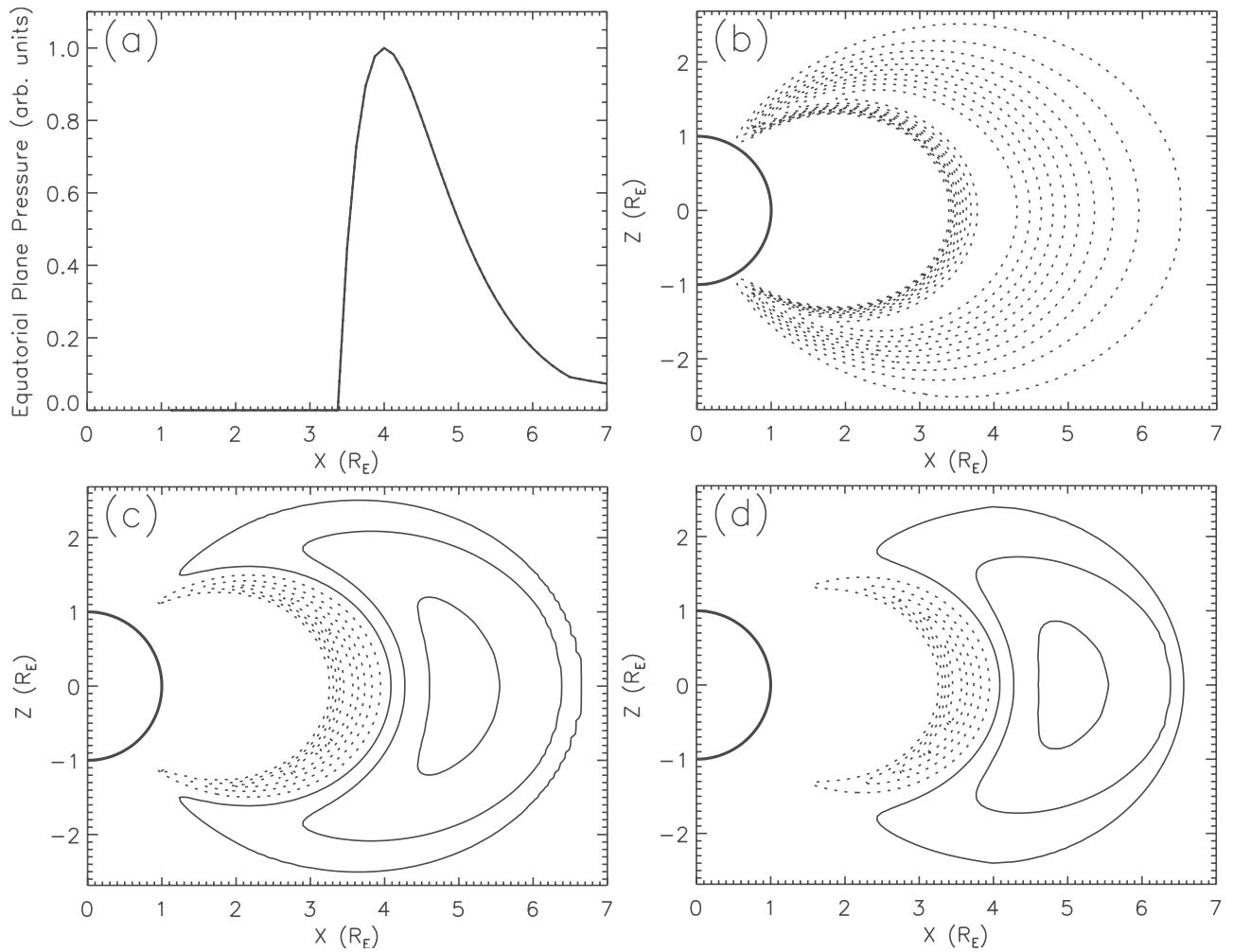
Figure 8. Same four panels as Figure 3, but for an isotropic pressure distribution with a real L shell dependence, with an adiabatic pressure profile extending into several ghost cells beyond the outer boundary of the integration volume.
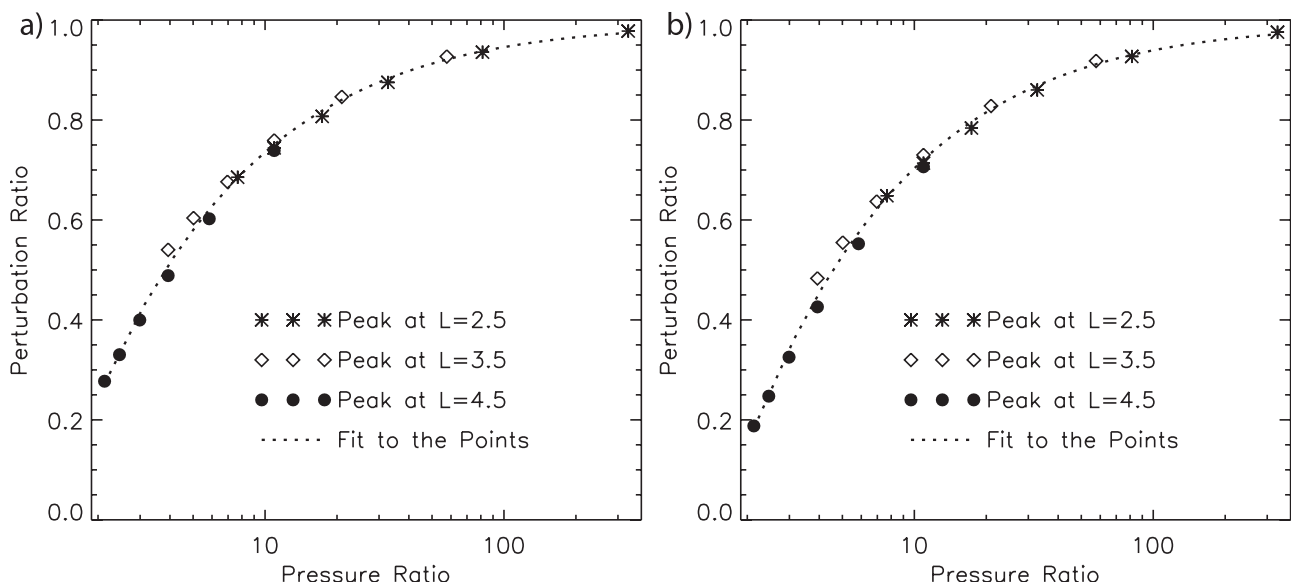

Figure 9. Magnetic perturbation ratio versus pressure ratio, as described in the text, for (a) an isotropic pressure distribution and (b) a pancake pressure distribution, with many parameter settings in the real L shell dependence profile formula.

Table 1. *Pr* and *Br* Values of the Fitted Relationships

Quantity	$P_\perp = P_\parallel$ Value	$P_\perp = 2P_\parallel$ Value
$Pr(Br = 0.0)$	1.277	1.544
$Pr(Br = 0.5)$	3.825	4.570
$Pr(Br = 0.9)$	41.00	48.30
$Br(Pr = 10.0)$	0.7355	0.7032

pressure ratio of 10.0. This is a typical pressure ratio, indicating that 25–30% of the total magnetic perturbation predicted by the DPS relation is from the truncation current and therefore not really from the pressure distribution inside the integration volume.

[28] In examining pressure profiles from observations and numerical experiments, the pressure ratio (for an outer boundary at geosynchronous orbit) is typically around 10–15 during quiet times. It then moves to lower values, perhaps as low as 4–5, during the main phase injection of the stormtime ring current. Finally, during the recovery phase of a magnetic storm, when the ring current is still enhanced but the plasma sheet ion population has returned to normal, P_r can increase to values as high as 40 (or more, in rare cases). Therefore there is a systematic progression along the curves shown in Figure 9 during the course of a magnetic storm, with the DPS relation being an excellent predictor of magnetic perturbation (from the particles inside the integration volume) during the recovery phase but a particularly bad predictor of this quantity during the main phase (that is, the truncation current is significantly, perhaps dominantly, contributing to the ΔB_{DPS} value).

[29] The significance of this result is that the overprediction of the perturbation inherent in the DPS relation is a systematic error that can be taken into account through a simple pressure ratio. The robustness of the result is validated by the number of cases contributing to each line (that is, each point in Figure 9 is a uniquely shaped pressure profile in the inner magnetosphere).

4.3. Further Analysis of the DPS Relation

[30] By varying other parameters of the pressure distribution, additional revelations about the DPS relation can be made. One such variation is in the pressure anisotropy. Figure 10 shows the dependence of $\Delta B_{BSI}/\Delta B_{DPS}$ on $P_\perp/P_\parallel$ for the nominal real pressure distribution. It is seen that for pancake distributions the perturbation ratio slowly rises to just above unity and appears to be asymptoting. For cigar-shaped distributions the ΔB ratio quickly drops. This is a numerical confirmation of the *Sckopke* [1966] generalization of the original *Dessler and Parker* [1959] study. *Sckopke* [1966] noted that the DPS relation is valid for a plasma distribution function with the form $f \propto \sin^\gamma\alpha$, with $\gamma \geq 0$. The present study goes a step further, showing that the DPS relation systematically overpredicts the true perturbation when $\gamma < 0$ (that is, for $P_\parallel > P_\perp$). In other words, it is not that the DPS relation's validity for $\gamma < 0$ is uncertain; it is certainly invalid.

[31] This overprediction can be explained by considering Figure 1. For a cigar-shaped distribution, the pressure along the field line maximizes away from the equator. Off equatorial currents, however, split their perturbation between a z component and an x-y component. This split is not taken into account in the DPS relation. It is believed that the systematic error seen in Figure 4 is primarily due to the overprediction of the axial perturbation from off equatorial currents. Figure 10 can be used as a general guideline for correcting the DPS relation for the average plasma anisotropy. Note, however, that this curve is for a specific spatial distribution of the pressure and assumes the same plasma anisotropy everywhere in the equatorial plane.

[32] Another parametric variation that can be investigated is the local time asymmetry of the pressure distribution. To thoroughly examine this effect, the ΔB calculation was performed not only at the Earth's center but also at 24 locations (every hour in MLT) around the equator of the Earth's surface ($L = 1$). Figure 11 shows these results for two different asymmetry configurations. Figure 11a is for a sine wave pressure amplitude around the nightside (zero from 0600 to 1800 MLT) and Figure 11b is for a delta function spike at 0000 MLT. Both calculations used an isotropic pressure with the nominal L shell variation as defined above. The values are normalized by $|\Delta B_{DPS}|$ to show the correct sign of the perturbation as a function of local time. In Figure 11, only the perturbation from the azimuthal currents in the inner magnetosphere is included in the results; the influence of the closure currents is discussed below. Even though both distributions yield a ΔB that is asymmetric in MLT, the average of the 24 values around the Earth is amazingly similar to the ΔB value at the center of the Earth. For the results in Figure 11a, $\Delta B_{BSI}(0)/\Delta B_{DPS}$ is 0.926223 while $\langle\Delta B_{BSI}(L = 1)\rangle/\Delta B_{DPS}$ is 0.926825. For the delta function results in Figure 11b, these two ratios are 0.926223 and 0.926830, respectively. Note that the influence from induced currents inside the Earth are not included in Figure 11 or in these ratios. For comparison, these ratios for an azimuthally symmetric pressure distribution are 0.926224 and 0.926834, respectively. These are all well within the uncertainty level of the numerical integration algorithm. So even though the DPS relation neglects the closure currents of the asymmetric ring current (remember that these currents are also neglected in the BSI results for a direct comparison), the DPS relation captures all of the perturbation from the magnetospheric azimuthal currents. This is also an expected result from the original derivation of the DPS relation, because the volume elements were not a priori defined to be azimuthally symmetric (symmetry was assumed only so that all of the current was included in the calculation).
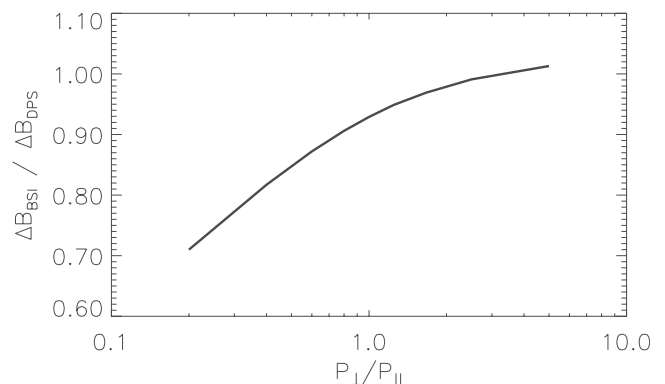

Figure 10. Ratio of ΔB_{BSI} to ΔB_{DPS} as a function of $P_\perp/P_\parallel$ for an isotropic pressure distribution with a real L shell dependence.
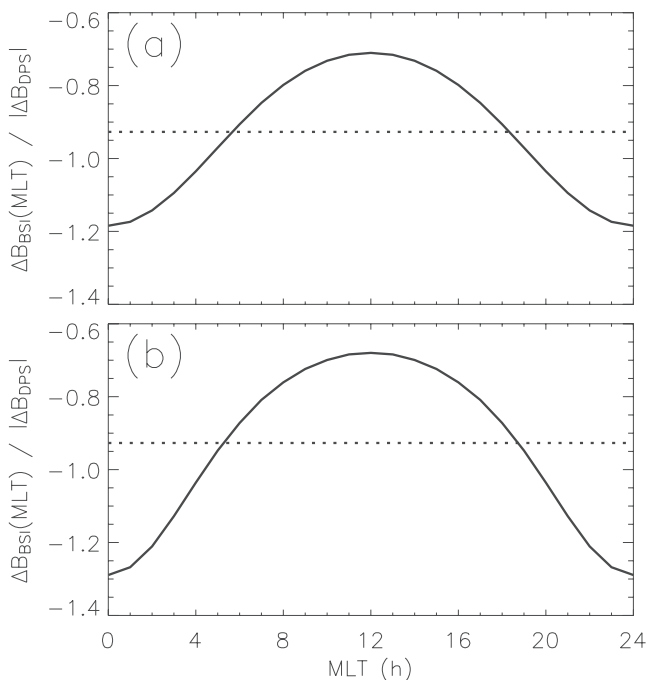
Figure 11. Ratio of ΔB_{BSI} to $|\Delta B_{DPS}|$ as a function of MLT for (a) a broad asymmetric distribution (sine wave dependence on the nightside, zero on the dayside) and for (b) a delta function in MLT at midnight. The pressure is isotropic with a nominal real L dependence (as in other figures). The solid line is the ratio for ΔB_{BSI} values as calculated at a chain of virtual magnetometers located every hour in MLT around the equator of the Earth (that is, at $L = 1$) and the dotted line is ratio for the average of these values.

[33] It is interesting to note that the magnitude of the ΔB asymmetry ($\Delta B_{max} - \Delta B_{min}$) is quite similar for the two pressure distributions, with values of 0.474 and 0.609 for Figures 11a and 11b, respectively. This result can be understood by examining the radial displacement $\mathbf{R} = \mathbf{r} - \mathbf{r}'$ dependence of the Biot-Savart law (equation (3)). With $\mathbf{R}$ in the numerator and $|\mathbf{R}|^3$ in the denominator, there is a net $\mathbf{R}^{-2}$ dependence of ΔB. An illustrative calculation to perform is to put a delta function of current (a spike in all three spatial coordinates) in the equatorial plane and then calculate the ΔB values on the nearside and farside of the Earth. The results of this exercise are shown in Figure 12. It is seen that the average of these two ΔB values is larger than their difference for $\mathbf{R} > 3.5$. Because this is a delta function of current, this is the maximum possible asymmetry. As the current is extended in local time, the total asymmetry decreases, eventually reaching zero for a uniform ring of current around the Earth. Therefore observations of asymmetries on the order of the average perturbation are most likely from very-near-Earth, localized currents. The most obvious possibilities are field-aligned and ionospheric currents.

[34] Let us briefly examine the current closure. The discussions of Figures 11 and 12 are incomplete in that the field-aligned and ionospheric closure currents of the azimuthally asymmetric perpendicular currents in the magnetosphere are neglected. This means that the values plotted

in Figures 11 and 12 implicitly include a closure current configuration that yields no net ΔB contribution [e.g., *Vasyliunas*, 1999]. Such a configuration may be unrealistic. Using the formulas in Appendix A, a complete calculation for the entire current loop can be performed. Figure 13 shows the normalized ΔB ($\Delta B_{BSI}(MLT)/|\Delta B_{DPS}|$) for three current segments (magnetospheric perpendicular currents, magnetospheric parallel currents, and ionospheric perpendicular currents) as well as the perturbation from the entire current loop. As in Figure 11, Figures 13a and 13c show results for a "broad" asymmetric pressure distribution (sine wave dependence across the nightside), while Figures 13b and 13d show the results for a delta function spike at midnight. The left-and right-hand plots show results with two different assumptions regarding the ionospheric closure of the partial ring current. Figures 13a and 13b show results for a nightside electrojet (that is, east-west directed) of current in the ionosphere with $J_{iono} = 0$ at noon. Figures 13c and 13d show results for the other extreme, with the current closing in a zonal electrojet around the dayside ionosphere with $J_{iono} = 0$ at midnight. The resulting MLT-averaged perturbations for each of these segments are given in Table 2. In all cases the field-aligned currents contribute substantially to the observed local time asymmetry but do
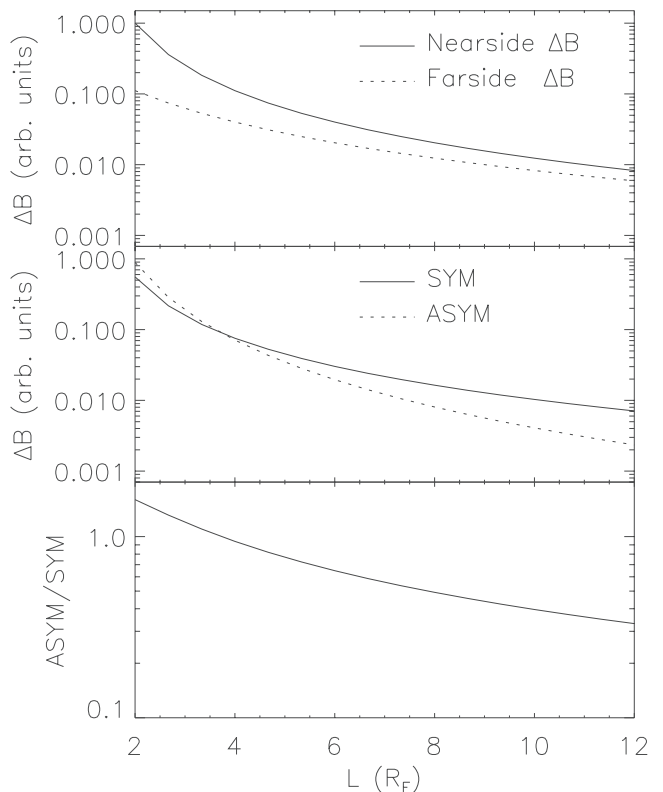

Figure 12. Parameters relating to the perturbation from a delta function of current a distance L from the center of Earth. (top) Perturbation as seen by a virtual magnetometer on the nearside of the Earth and that seen by one on the farside of the Earth (both at the equator). (middle) The average of the nearside and farside perturbation values (*SYM*, solid line) and the ratio of the nearside value to the farside value (*ASYM*, dotted line). (bottom) The ratio of *ASYM* to *SYM*.
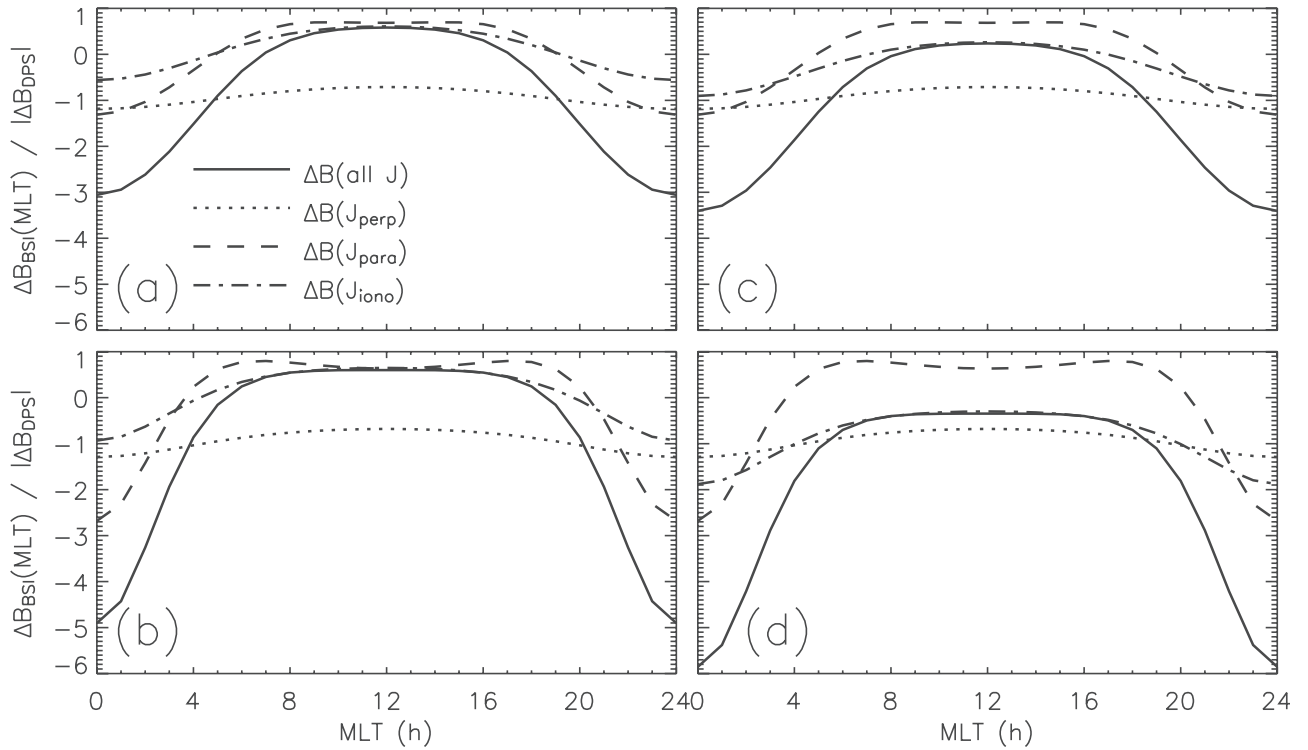
Figure 13. The ratio of ΔB_{BSI} to $|\Delta B_{DPS}|$ as a function of MLT (as in Figure 11) for (a and c) a broad asymmetric distribution and (b and d) a delta function in MLT at midnight. Shown are the perturbations from the magnetospheric current segments (dotted line), the field-aligned current segments (dashed line), the ionospheric current segments (dash-dotted line), and the entire current loop (solid line). Results from two different assumptions about the closure are shown, with the ionospheric currents flowing zonally across the nightside (Figures 13a and 13b) with $J_{iono} = 0$ at noon and across the dayside (Figures 13c and 13d) with $J_{iono} = 0$ at midnight.

not influence the MLT-averaged value (given our configuration of currents and virtual magnetometers). Because the ionospheric currents have a net flow from the dusk side of the planet to the dawn side of the planet, they also contribute to the local time asymmetry in the same sense as the magnetospheric and field-aligned current segments (negative on the nightside and positive on the dayside). Depending on the direction of the ionospheric closure, however, the contribution to the MLT-averaged value can be either positive or negative. When the currents close across midnight, most of the magnetometers see a positive perturbation, and so the average is the opposite sense as the magnetospheric segment. This is similar to the *Crooker and Siscoe* [1974] result of ~20% of the perturbation from a model partial ring current resulting from the eastward electrojet in the ionosphere. When the currents close across noon, the reverse is true, and the average perturbation is in the same sense as that from the magnetospheric currents. It is seen that nearly all of the local time asymmetry is due to the currents that are close to the Earth, while a majority of the globally averaged perturbation is from the perpendicular currents in the magnetosphere. Of course, these are simply idealized examples of pressure asymmetries in the inner magnetosphere with simplistic assumptions about the nature of the closure current. Allowing north-south closure in the ionosphere would certainly change the resulting perturba-

tion. It should be noted that the ΔB asymmetry for the entire current loop perturbation profiles shown in Figures 13a–13d are 3.641, 5.503, 3.644, and 5.508, respectively (normalized to ΔB_{DPS}). Asymmetries of this size are never observed (e.g., examine *SYM-H* and *ASY-H* available online at the World Data Center for Geomagnetism at http://swdcwww.kugi.kyoto-u.ac.jp/index.html, which show that *ASY-H* rarely exceeds $|SYM-H|$). So these idealized cases are either unrealistic and/or not a complete set of relevant currents. For a real event study a robust conductance model should be used to solve Poisson's equation to get the true ionospheric current pattern for each time throughout the event including high-latitude currents, which will presum-

Table 2. Magnetic-Local-Time-Averaged Perturbations[a]

Segment	Broad Peak	Narrow Peak
All J (nightside J_{iono})	0.8146	0.8146
All J (dayside J_{iono})	1.161	1.762
J_{perp} only	0.9268	0.9269
J_{para} only	0.000	0.000
J_{iono} only, nightside jet	−0.1123	−0.1123
J_{iono} only, dayside jet	0.2341	0.8334

[a]Normalized by ΔB_{DPS} for the current segments in the azimuthally asymmetric configurations of the pressure distribution (as shown in Figure 13).

ably cancel much of the asymmetry from the midlatitude currents.

5.   Discussion and Conclusions

[35]   The main finding of this study is that the truncation current, which is implicitly included in the DPS relation whenever the plasma pressure is nonzero at the outer boundary, causes the DPS relation to overpredict the size of the perturbation from the particle energy inside the integration volume. This truncation current is introduced because the DPS relation assumes that all of the plasma pressure is contained within the integration volume. If it is not, then the DPS relation introduces ghost cells of zero pressure at the outer edge of the volume and then includes in its total magnetic perturbation the contribution from the large azimuthal current associated with this pressure truncation. As shown above, the perturbation from this non-physical current can be significant, but there is a simple formula relating this error to the ratio of the peak pressure to that at the boundary.

[36]   Some studies report that *Dst* can be well predicted by the DPS relation using only the inner magnetospheric ion energy content, while others say that additional currents must be taken into account. For instance, *Greenspan and Hamilton* [2000] showed experimentally that the DPS relation works well. Other studies, such that of as *Roeder et al.* [1996], showed that a DPS integral of observed ion fluxes were only able to account for 40–70% of the observed *Dst* value, but this study used data that have a lower energy cutoff of 40–50 keV, which misses a significant portion of the ring current ions [see, e.g., *Liemohn and Kozyra*, 2002]. Modeling results also predict most or all of the observed *Dst** with a DPS conversion of the total energy content in the simulation results [e.g., *Jordanova et al.*, 1998; *Kozyra et al.*, 1998; *Liemohn et al.*, 1999]. Studies that contradict this equity are those that predict a non-negligible contribution to *Dst* from other currents. The tail current is one that has received attention recently, with predictions of 25–50% of the *Dst* perturbation from this system [*Alexeev et al.*, 1996; *Turner et al.*, 2000, 2001; *Ohtani et al.*, 2001]. The question, then, is how to reconcile these seemingly contradictory results regarding the formation of *Dst*.

[37]   The present study provides a possible answer to this dilemma. The truncation current implicitly included in the DPS relation is, in some qualitative sense, accounting for the tail current or any current beyond the outer boundary (that is, it could even be additional symmetric or partial ring current). The perturbation from the truncation current is, of course, just an estimate of the perturbation from any real currents beyond the integration volume because the magnetic field quickly becomes nondipolar and dynamic. However, the overprediction of the DPS relation can be thought of as a crude estimate of the contribution from these other currents. Because typical ring current pressure profiles have P_r values of 10–20, the typical truncation error is 20–30% of the DPS perturbation value. This number roughly matches the estimates of the contribution to the *Dst* index from tail currents and other currents beyond geosynchronous orbit. Therefore using the DPS relation for the energy content of only the ring current and then directly comparing

it against *Dst** (*Dst* corrected for the magnetopause currents, quiet time offsets, and induced currents in the Earth) is probably an acceptable proxy for the contribution from the ring current and the tail current combined.

[38]   It is useful to compare this result with the more general form of the DPS relation derived from the virial theorem [*Olbert et al.*, 1968; *Siscoe*, 1970]

$$\frac{\Delta B(0)}{B_E} = -\frac{2E_{RC} + U_{RC} + U_i + U_b - \oint p_t \mathbf{r} \cdot \mathbf{n} d\sigma}{3U_E} \quad (13)$$

In equation (13), U_{RC} is the magnetic energy of the ring current, U_i is the magnetic interaction energy between the Earth and the ring current, U_b is the magnetic energy associated with the boundary currents, and the integral is the boundary current term. In this study, U_{RC} and U_i are assumed to be small compared to E_{RC}. The question that arises as to the relationship between the truncation currents discussed in this paper and the boundary currents included in equation (13). The fundamental difference is that the boundary current in equation (13) is assumed to be generated by a nonzero pressure outside of the integration volume (with zero pressure immediately inside the boundary). Such a pressure configuration produces a positive magnetic perturbation in and on the Earth. This is the situation on the dayside magnetopause, with a quiet time magnitude of 10–20 nT and peak values in the range 50–100 nT [e.g., *Burton et al.*, 1975; *O'Brien and McPherron*, 2000; *Vasyliunas*, 2001]. In the present study the situation is reversed; there is a nonzero pressure immediately inside the volume boundary and a zero-pressure level beyond it. This reversal results in a negative contribution to the perturbation at Earth. To the best of our knowledge the perturbation from such a pressure configuration has never been discussed. Therefore, while the concept of a boundary current contribution to the magnetic perturbation at Earth is not new, this particular manifestation of the boundary current is new, and so this study presents yet another caveat to using the DPS relation.

[39]   As a final note, the role of the field-aligned and ionospheric current contributions to ΔB have not been rigorously addressed in this study. These currents arise not only from the closure of the partial ring current within the integration volume of the inner magnetosphere, but also from the region 1 and region 2 currents flowing into and out of the ionosphere at higher latitudes. While the method presented above is flexible enough to handle these currents, the ionospheric current closure requires accurate knowledge of the ionospheric conductances, particularly those in the subauroral nightside, of which very little is known. In this study, it was shown that the closure currents always contribute to the local time profile of the magnetic perturbation, but the contribution to the globally averaged perturbation can be either large or small and either positive or negative. Others have found that the closure current contribution is largely from the Hall current [e.g., *Siscoe and Crooker*, 1974; *Chen et al.*, 1982], which was not considered in this study. Another contributor is the longitudinal offset between region 1 and region 2 currents, which also causes a dawn-dusk asymmetry but very little globally averaged (i.e., *Dst*) influence [e.g., *Crooker and Siscoe*, 1981]. During storms this offset will increase owing to twisting of both patterns,

and the asymmetry can get even larger. In conclusion, an accurate calculation of any of these influences requires a self-consistent solution. It was the point of this study to show the influence of the truncation current, which can be significant, and the details of the perturbation from these other currents are left for future investigations.

Appendix A: Biot-Savart Law Integration

[40] Given an array of virtual magnetometer stations (indexed below as n) each at a position $\mathbf{r}_n$, the north-south (H) component of the perturbation field generated by a current density throughout a volume $V(\mathbf{r}')$ can be found from equation (3). For this calculation, V will be dissected into an arbitrarily large array of grid cells in L', φ', and λ' (indexed below as i, j, and k). Note that while the grid is in dipolar coordinates (chosen for ease in distribution function mapping), the vector variables at these locations are often specified in terms of Cartesian coordinate directions (chosen for ease in vector manipulations). Also, in dipolar coordinates,

$$r' = R_E L' \cos^2 \lambda' \tag{A1}$$

is the dependence of geocentric radial distance of L shell on latitude.

[41] The main text discussed the calculation of the perpendicular current densities in the magnetosphere. The current densities parallel to the magnetic field lines are found from the divergence of $\mathbf{I}_\perp$ (current, not current density)

$$\mathbf{B} \cdot \nabla \left(\frac{J_\parallel}{B} \right) = \nabla \cdot \mathbf{J}_\perp, \tag{A2}$$

which is accumulated along the field line. These field-aligned currents can have a positive or negative flow along $\mathbf{B}_0$, and in fact it often has opposite signs in the two hemispheres along the same field line. These parallel current densities are used as a source term in Poisson's equation for the ionospheric potential Φ [e.g., *Vasyliunas*, 1970]

$$\nabla(-\Sigma \nabla \Phi) = J_\parallel \sin\psi, \tag{A3}$$

where Σ is the height-integrated ionospheric conductance tensor and ψ is the magnetic field inclination angle. Once a spatial distribution of Φ is known from equation (A3), the ionospheric Pedersen and Hall currents can be defined using Ohm's law,

$$\mathbf{J}_{\mathrm{iono}} = -\Sigma \nabla \Phi. \tag{A4}$$

[42] The perturbation from any of the currents defined by equations (4), (A2), or (A4) can be written out in index notation as follows,

$$\Delta H_a(n) = \sum_{i,j,k} C_{\Delta H} \left\{ \cos\lambda_n \left(J_x R_y - J_y R_x \right) \sin\lambda_n \left[\cos\varphi_n \left(J_y R_z - J_z R_y \right) \right. \right.$$
$$\left. \left. + \sin\varphi_n (J_z R_x - J_x R_z) \right] \right\}, \tag{A5}$$

where the sine and cosine terms are included to select the H component of the perturbation. The relative position vector, $\mathbf{R} = \mathbf{r} - \mathbf{r}'$, is given by

$$R_\xi = r_\xi(n) - r'_\xi(i,j,k)$$
$$\xi = x, y, z, \tag{A6}$$

where the components of $\mathbf{r}$ (location of the virtual magnetometer) can be defined from a Cartesian, spherical, or dipolar perspective, but the components of $\mathbf{r}'$ (location of the current) is defined by a transformation from dipolar coordinates and $C_{\Delta H}$ has this form for the magnetospheric currents ($\mathbf{J}_\perp$ and $J_\parallel$)

$$C_{\Delta H}(\mathbf{r}') = \frac{\mu_0}{4\pi} \sqrt{\frac{B_{eq}(i)}{B(i,k)}} \frac{R_E L'(i) \cos^3 \lambda' \Delta s(i,k) \Delta r_{eq} \Delta\varphi}{\left(R_x^2 + R_y^2 + R_z^2 \right)^{3/2}} \tag{A7a}$$

and the following form for $\mathbf{J}_{\mathrm{iono}}$:

$$C_{\Delta H}(\mathbf{r}') = \frac{\mu_0}{4\pi} \frac{r'^2 \cos\lambda' \Delta s_{\mathrm{iono}} \Delta \Lambda_{\mathrm{iono}}(\mathbf{r}') \Delta\varphi}{\left(R_x^2 + R_y^2 + R_z^2 \right)^{3/2}}. \tag{A7b}$$

In equation (A7) the subscript "eq" denotes the value is taken at the equatorial plane, and the subscript "$iono$" indicates that the value is taken at the ionosphere. Also, the volume element has been given several forms, such as

$$d\mathbf{r}' = (\Delta r)(r' \cos\lambda' \Delta\varphi)(r' \Delta\lambda)$$
$$= \left(\sqrt{\frac{B_{eq}}{B}} \Delta r_{eq} \right) (L' R_E \cos^3 \lambda' \Delta\varphi)(\Delta s). \tag{A8}$$

Note that both hemispheres (northern and southern) must be included in the integration domain, including the conjugate ionospheres for each field line. It should also be pointed out that equation (A5) yields ΔH in units of nT given J in nanoamperes per squared meter and all distances in m. In equation (A7a), Δs is the length of the grid cell along the field line and is determined by a cell-centered difference using equation (A1). In (A7b), Δs_{iono} is the vertical extent of the ionospheric currents, which will eventually cancel out of the formulation. Also in equation (A7b), $\Delta \Lambda_{\mathrm{iono}}$ is the ionospheric projection of Δr_{eq}.

[43] Let us now consider how to obtain the currents from the various formulas in section 3. For equation (4) the calculation of the gradient curvature component of this current is straightforward,

$$J_{\xi_1,GC} = \frac{\left[P_\parallel(i,j,k) - P_\perp(i,j,k) \right]}{B^3(i,k)} \left[B_{\xi_2}(i,k) \frac{\partial B(i,k)}{\partial \xi_3} - B_{\xi_3}(i,k) \frac{\partial B(i,k)}{\partial \xi_2} \right], \tag{A9}$$

where ξ_1, ξ_2, and ξ_3 cycle through x, y, and z for each vector direction. Because $\mathbf{B}$ is assumed to be dipolar, its spatial derivatives can be expressed analytically. The magnetization term, however, requires a Cartesian coordinate derivative of $P_\perp$,

$$J_{\xi_1,M} = \frac{B_{\xi_2}(i,k)}{B^2(i,k)} \frac{\partial P_\perp(i,j,k)}{\partial \xi_3} - \frac{B_{\xi_3}(i,k)}{B^2(i,k)} \frac{\partial P_\perp(i,j,k)}{\partial \xi_2}, \tag{A10}$$
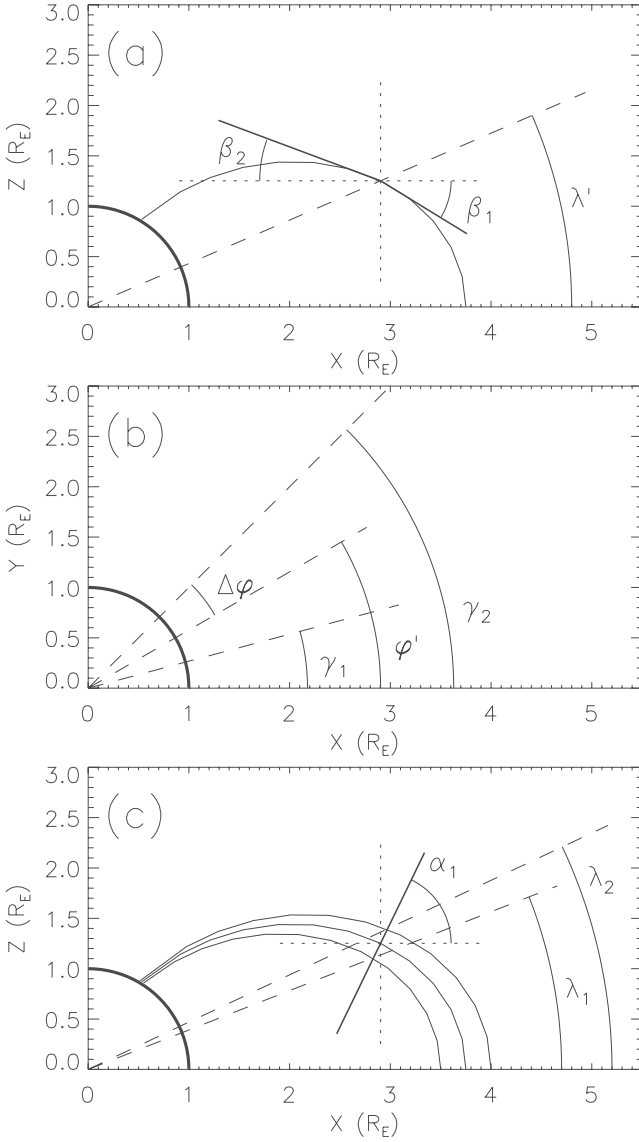
Figure A1. Geometries for the angle definitions used in the calculation, with schematics showing (a) β_1, β_2, and λ' in the X-Z plane; (b) φ', $\Delta\varphi$, γ_1, and γ_2 in the X-Y plane; and (c) λ_1, λ_2, and α_1 in the X-Y plane.

which will have to be performed numerically. However, the derivative of $P_\perp$ on the dipolar grid is straightforward, and these can be converted into the needed values. Figure A1 shows the geometry between a grid cell and its nearest neighbors for the three dipolar coordinate directions. In Figure A1a, Δs_1 and Δs_2 are defined similarly to Δs above and β_1 and β_2 are the angles (with respect to the x-y plane) to the southern and northern neighboring cells along the field line, respectively, and can be written as

$$\beta_1 = \text{atan}\left[\frac{B_z(i,k) + B_z(i,k-1)}{B_{xy}(i,k) + B_{xy}(i,k-1)}\right]$$

$$\beta_2 = \text{atan}\left[\frac{B_z(i,k) + B_z(i,k+1)}{B_{xy}(i,k) + B_{xy}(i,k+1)}\right], \tag{A11}$$

where the "xy" subscript denotes the component of the vector in the x-y plane. In Figure A1b, γ_1 and γ_2 are the angles (with respect to the x-z plane) to the western and eastern neighboring cells, respectively, and can be written as

$$\gamma_1 = \varphi'(j) - .5\Delta\varphi$$

$$\gamma_2 = \varphi'(j) + .5\Delta\varphi. \tag{A12}$$

In Figure A1c, α_1 is the angle normal to the local geomagnetic field (in the direction of decreasing B) and can be written as

$$\alpha_1 = \begin{cases} \text{asin}\left[\frac{B_z(i,k)}{B(i,k)}\right] - \frac{\pi}{2}, & \lambda < 0 \\ \frac{\pi}{2} - \text{asin}\left[\frac{B_z(i,k)}{B(i,k)}\right], & \lambda \geq 0. \end{cases} \tag{A13}$$

Also in Figure A1c, $\Delta r = \Delta r_{eq} \cos^3 \lambda'$ is the distance between field lines along α_1 in each direction and λ_1 and λ_2 are the latitude of the intersection of the normal vectors with the inner and outer field lines, respectively, defined as

$$\lambda_1 = \text{atan}\left[\frac{r'_z(i,j,k) - \Delta r \sin\alpha_1}{r'_{xy}(i,j,k) - \Delta r \cos\alpha_1}\right] \tag{A14a}$$

$$\lambda_2 = \text{atan}\left[\frac{r'_z(i,j,k) + \Delta r \sin\alpha_1}{r'_{xy}(i,j,k) + \Delta r \cos\alpha_1}\right] \tag{A14b}$$

Given this geometry, the dipolar coordinate derivatives of $P_\perp$ can be written as follows:

$$dP_i = [\chi_2 P_\perp(i+1,j,k(\lambda_2)) + (1-\chi_2)P_\perp(i+1,j,k(\lambda_2)-1)]$$

$$- [\chi_1 P_\perp(i-1,j,k(\lambda_1)) + (1-\chi_1)P_\perp(i-1,j,k(\lambda_1)-1)] \tag{A15a}$$

$$dP_{j1} = P_\perp(i,j,k) - P_\perp(i,j-1,k) \tag{A15b}$$

$$dP_{j2} = P_\perp(i,j+1,k) - P_\perp(i,j,k) \tag{A15c}$$

$$dP_{k1} = P_\perp(i,j,k) - P_\perp(i,j,k-1) \tag{A15d}$$

$$dP_{k2} = P_\perp(i,j,k+1) - P_\perp(i,j,k), \tag{A15e}$$

where $k(\lambda_1)$ and $k(\lambda_2)$ are indices of the closest cell (to the north) to λ_1 and λ_2 along those field lines, respectively, and χ_1 and χ_2 are interpolation factors

$$\chi_1 = \frac{\lambda'(i-1,k(\lambda_1)) - \lambda_1}{\lambda'(i-1,k(\lambda_1)) - \lambda'(i-1,k(\lambda_1)-1)} \tag{A16a}$$

$$\chi_2 = \frac{\lambda(i+1,k(\lambda_2)) - \lambda_2}{\lambda(i+1,k(\lambda_2)) - \lambda(i+1,k(\lambda_2)-1)}. \tag{A16b}$$

Note that equation (A16a) does not need to be used if $P_\perp$ can be calculated exactly at λ_1 and λ_2. Using equations (A11)–(A14), the difference values in equation (A15) can then be converted into Cartesian coordinate derivatives as follows:

$$\frac{\partial P_\perp}{\partial x} = \frac{1}{2}\left(\frac{\Delta P_i \cos\alpha_1 \cos\varphi'}{\Delta r} + \frac{\Delta P_{k,i}\cos\beta_1\cos\varphi'}{\Delta s_1} + \frac{\Delta P_{k,2}\cos\beta_2\cos\varphi'}{\Delta s_2} - \frac{\Delta P_{j,1}\cos\gamma_1 + \Delta P_{j,2}\cos\gamma_2}{2r'_{xy}(i,k)\Delta\varphi}\right) \quad \text{(A17a)}$$

$$\frac{\partial P_\perp}{\partial y} = \frac{1}{2}\left(\frac{\Delta P_i \cos\alpha_1 \sin\varphi'}{\Delta r} + \frac{\Delta P_{k,i}\cos\beta_1\sin\varphi'}{\Delta s_1} + \frac{\Delta P_{k,2}\cos\beta_2\sin\varphi'}{\Delta s_2} + \frac{\Delta P_{j,1}\cos\gamma_1 + \Delta P_{j,2}\cos\gamma_2}{2r'_{xy}(i,k)\Delta\varphi}\right) \quad \text{(A17b)}$$

$$\frac{\partial P_\perp}{\partial z} = \frac{1}{2}\left(\frac{\Delta P_i \sin\alpha_1}{\Delta r} + \frac{\Delta P_{k,1}\sin\beta_1}{\Delta s_1} + \frac{\Delta P_{k,2}\sin\beta_2}{\Delta s_2}\right), \quad \text{(A17c)}$$

which can be used in equation (A10).

[44] For $J_\parallel$ the value of $J_\perp$ at the cell interface is determined by an interpolation of the nearest neighbors. From equations (A9) and (A10), $J_\perp$ is known in Cartesian coordinates on the dipolar grid, and using the geometry in Figure A1, the Cartesian vectors at the interfaces can be written as

$$J_{i-1/2,\xi} = \frac{1}{2}\left[J_{\perp,\xi}(i,j,k) + \chi_1 J_{\perp,\xi}(i-1,j,k(\lambda_1))-1)+(1-\chi_1) \cdot J_{\perp,\xi}(i-1,j,k(\lambda_1))\right] \quad \text{(A18a)}$$

$$J_{i+1/2,\xi} = \frac{1}{2}\left[J_{\perp,\xi}(i,j,k) + \chi_2 J_{\perp,\xi}(i+1,j,k(\lambda_2))-1)+(1-\chi_2) \cdot J_{\perp,\xi}(i+1,j,k(\lambda_2))\right] \quad \text{(A18b)}$$

$$J_{j-1/2,\xi} = \frac{1}{2}\left[J_{\perp,\xi}(i,j,k) + J_{\perp,\xi}(i,j-1,k)\right] \quad \text{(A18c)}$$

$$J_{j+1/2,\xi} = \frac{1}{2}\left[J_{\perp,\xi}(i,j,k) + J_{\perp,\xi}(i,j+1,k)\right], \quad \text{(A18d)}$$

and so $J_{\perp,ij\pm1/2} = \pm\mathbf{J}_{ij\pm1/2} \cdot \hat{\mathbf{n}}_{ij\pm1/2}$ can be written from equation (A18) as

$$J_{\perp,i\pm1/2} = \pm J_{i\pm1/2,x}\cos\alpha_1\cos\varphi' \pm J_{i\pm1/2,y}\cos\alpha_1\sin\varphi' \pm_{i\pm1/2,z}\sin\alpha_1 \quad \text{(A19a)}$$

$$J_{\perp,j\pm1/2} = \mp J_{j\pm1/2,x}\sin\gamma_1 \pm J_{j\pm1/2,y}\cos\gamma_1. \quad \text{(A19b)}$$

In addition, the surface areas of the cell faces are given by

$$A_{\perp,j\pm1/2} = \left(\sqrt{\frac{B_{eq}}{B}}\Delta r_{eq}\right)(\Delta s)$$
$$A_{\perp,i\pm1/2} = \left(r'_{i\pm1/2}\cos\lambda'\Delta\varphi\right)(\Delta s_{i\pm1/2}), \quad \text{(A20)}$$

and the flux tube cross section can be written as

$$A_\parallel = (r'\cos\lambda'\Delta\varphi)\left(\sqrt{\frac{B_{eq}}{B}}\Delta r_{eq}\right). \quad \text{(A21)}$$

Using these definitions, the solution of $J_\parallel$ is clear. This scalar is then directed along **B** for use in equation (A5). For the final component of the current, $\mathbf{J}_{iono}$, its value from equation (A4) can be used directly in equation (A5), as discussed above.

Appendix B: Derivation of Pressure Formulas

[45] For collisionless mapping along a magnetic field line, the distribution function only depends on two constants of motion [*Whipple*, 1977], the total energy E

$$E = \frac{mv_\parallel^2}{2} + \frac{mv_\perp^2}{2} + \Pi \quad \text{(B1)}$$

and the first adiabatic invariant μ (slightly rewritten from equation (6))

$$\mu = \frac{mv_\perp^2}{2B}. \quad \text{(B2)}$$

In equation (B1), Π is the total potential energy, which includes the electrostatic potential Φ as well as other potential fields like gravity, centrifugal acceleration, or ponderomotive effects [see, e.g., *Khazanov et al.*, 1998]. The moments of the distribution can then be written in terms of these new variables E and μ,

$$P_\parallel = \left(\frac{2}{m}\right)^{3/2}\pi B \int\int\sqrt{E-\mu B - \Pi}f(E,\mu)dEd\mu \quad \text{(B3a)}$$

$$P_\perp = \frac{\sqrt{2}\pi B^2}{m^{3/2}}\int\int\frac{\mu f(E,\mu)}{\sqrt{E-\mu B - \Pi}}dEd\mu \quad \text{(B3b)}$$

The advantage of switching to these variables is that the distribution function is now invariant in E-μ space with position along the field line, and the proper moment values are obtained simply by integrating over a changing region of E-μ space. Figure B1a shows a typical integration region, which extends over the range of positive μ above a line defined by $E \geq \mu B + \Pi$ (i.e., the region where the particle kinetic energy K_E is greater than zero). Note that the integration must be doubled to account for both hemispherical directions in velocity space (or a second integration should be done for the oppositely flowing particle distribution). This technique was originally developed by *Whipple* [1977], but his formulation (and that of most others) is limited in applicability by a set of rather stringent criteria on the relationship between Π and B [*Chiu and Schulz*, 1978]. A more generalized approach of piecewise integration in E-μ space was developed by *Liemohn and Khazanov* [1998] and applied for geophysical topics by *Khazanov et al.* [1998].

[46] That technique that will be used here for mapping of the distribution functions and calculating the pressures. It
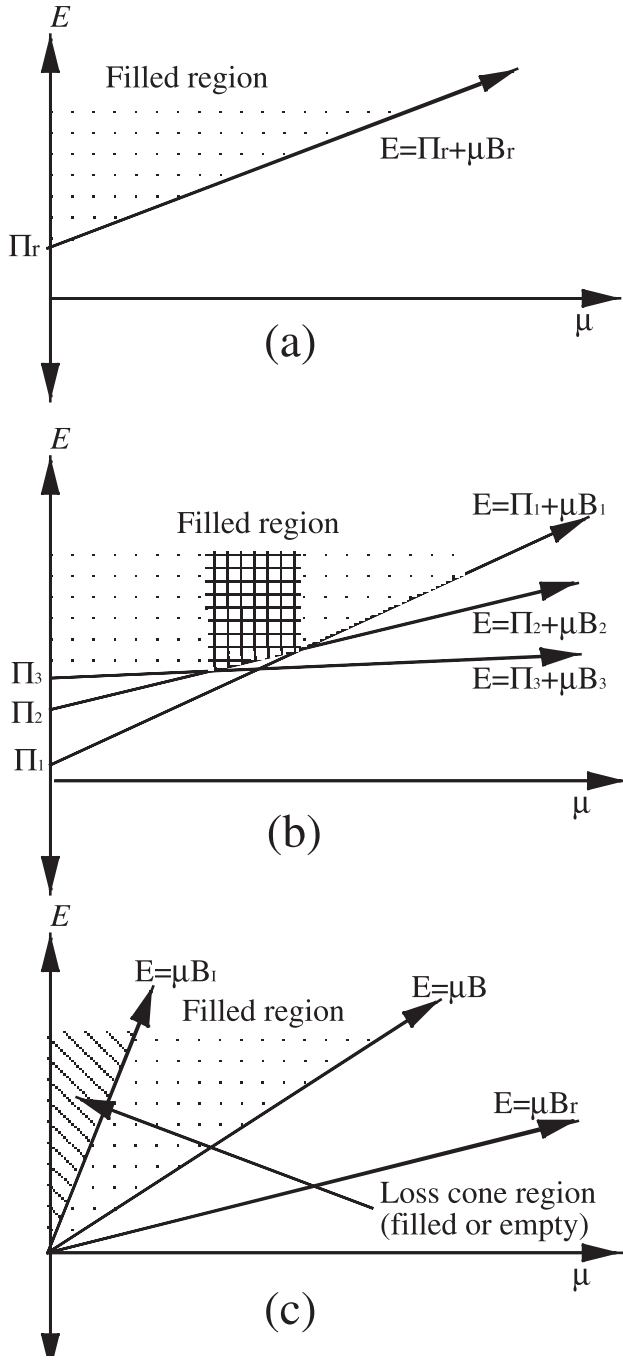
Figure B1. Schematics showing the filled and empty regions of velocity space in the E-μ plane for (a) a single baseline defining the lower integration limit, (b) an example of how three baselines can combine to form the lower integration limit, thus requiring three piecewise integrations to obtain a moment of the velocity distribution, and (c) the specific case for this study, showing the baseline at the reference altitude, the baseline at the local altitude, and the loss cone baseline that must be subtracted if assumed to be empty.

allows for an arbitrary Π distribution and B variation along the field line because it builds the total integral in equation (B3) from additive and subtractive summations of integrals over only a portion of E-μ space, each with simple boundary

conditions in E and μ. Figure B1b illustratively shows an E-μ region requiring several piecewise integrations. Any holes in velocity space (such as a loss cone) are included by subtracting away piecewise integrations over those regions of E-μ space. The additional lower boundary lines necessitating this piecewise approach arise owing to Π and B not satisfying the *Chiu and Schulz* [1978] criteria.

[47]   It will be assumed that the distribution is defined by a bi-Maxwellian function. In the chosen variables this function has the form

$$f = \left(\frac{m}{2\pi}\right)^{3/2} \frac{n_o(A+1)}{T_\parallel^{3/2}} \exp\left(-\frac{E - \Pi_o + \mu B_o A}{T_\parallel}\right), \qquad (B4)$$

where $A = T_\parallel/T_\perp - 1 = P_{\parallel r}/P_{\perp \rho} - 1$ is an anisotropy index of the parallel and perpendicular temperatures at the reference point along the field line (in this case, the equatorial plane). Also, n_r, Π_r, and B_r are the density, potential, and magnetic field strength at the reference point, respectively. Inserting equation (B4) into equation (B3) yields rather complicated expressions for the pressures

$$P_\parallel = \frac{n_r(A+1)B}{\sqrt{\pi}T_\parallel^{3/2}} \exp\left(\frac{\Pi_r}{T_\parallel}\right) \sum_a S_a \int\limits_{\mu=\mu_{a,1}}^{\mu_{a,2}} \exp\left(-\frac{\mu B_r A}{T_\parallel}\right)$$

$$\cdot \left[\int\limits_{E=\mu B_a + \Pi_a}^{\infty} \sqrt{E - \mu B - \Pi} \exp\left(-\frac{E}{T_\parallel}\right) dE\right] d\mu \qquad (B5a)$$

$$P_\perp = \frac{n_r(A+1)B^2}{2\sqrt{\pi}T_\parallel^{3/2}} \exp\left(\frac{\Pi_r}{T_\parallel}\right) \sum_a S_a \int\limits_{\mu=\mu_{a,1}}^{\mu_{a,2}} \mu \exp\left(-\frac{\mu B_r A}{T_\parallel}\right)$$

$$\cdot \left[\int\limits_{E=\mu B_a + \Pi_a}^{\infty} \frac{1}{\sqrt{E - \mu B - \Pi}} \exp\left(-\frac{E}{T_\parallel}\right) dE\right] d\mu \qquad (B5b)$$

where the summation over "a" runs over all of the piecewise integrals necessary to construct the "filled" velocity space region in E-μ space, and S_a is either plus or minus one depending on whether the piecewise integral should be added into the total integral or subtracted away from the total. The integration endpoints μ_{a1} and μ_{a2} are the intersection points of the $E = \mu B_a + \Pi_a$ line with the $E = \mu B_{a-1} + \Pi_{a-1}$ line and the $E = \mu B_{a+1} + \Pi_{a+1}$ line, respectively (left and right endpoints of the integration domain). The $E = \mu B_a + \Pi_a$ line defines the lower bound of the integration domain, which extends up to infinity in the E direction. Holes in the distribution are then created by subtracting other piecewise integrals from the region already included in the additive piecewise integrals. In addition, because of the square of the velocities in equations (B1) and (B2), there must be a set of "a" integrals for each direction along the field line, which may or may not have the same integration boundaries or distribution function (depending on the profile of B and Π along the field line and the boundary conditions on f).

[48]   Because a bi-Maxwellian was chosen, though, every piecewise integration in equation (B5), no matter what the complexity of B or Π, has an analytical solution [*Liemohn*

and Khazanov, 1998; *Khazanov et al.*, 1998]. An assumption that greatly simplifies the solution of equation (B5) is that the magnetic field lines are equipotentials (that is, $\Pi = 0$ everywhere). This not only eliminates terms in equation (B5), but it reduces the number of piecewise integrations to a minimum. For the case of a filled loss cone distribution, there is only a single "*a*" value, defined by the local magnetic field strength. For an empty loss cone distribution, another integration must be included in the scenario to subtract off this part of E-μ space. These integration boundaries are shown in Figure B1c.

[49] For a reference point at the equatorial plane, the solution to equation (B5) is given in the main text in equation (7) for the filled loss cone case and in equation (8) for the empty loss cone case. Note that this latter solution requires a modification of the equatorial values in equation (8), as shown in equation (9), in order to maintain the original pressure values at the reference point. Note that equation (8) has already taken into account a conversion of n_r to n_r^* for this equatorial plane value adjustment

$$n_r^* = n_r \sqrt{\frac{B_I + AB_r}{B_I - B_r}}. \tag{B6}$$

The reader is referred to *Whipple* [1977] for more information regarding the development and application of E-μ space, to *Chiu and Schulz* [1978] for information about the validity criteria for Liouville theorem mappings that only consider the endpoint values of B and Π, and to *Liemohn and Khazanov* [1998] and *Khazanov et al.* [1998] for a method to extend Liouville theorem mappings to an arbitrary B-Π relationship along the field line.

References

Ahn, B.-H., R. M. Robinson, Y. Kamide, and S.-I. Akasofu, Electric conductivities, electric fields, and auroral particle energy injection rate in the auroral ionosphere and their empirical relations to the horizontal magnetic disturbances, *Planet. Space Sci.*, *31*, 641, 1983.

Alexeev, I. I., E. S. Belenkaya, V. V. Kalegaev, Y. I. Feldstein, and A. Grafe, Magnetic storms and magnetotail currents, *J. Geophys. Res.*, *101*, 7737, 1996.

Alfvén, H., and C.-G. Fälthammar, *Cosmical Electrodynamics, Fundamental Principles*, Oxford Univ. Press, New York, 1963.

Baker, J., and J. Hurley, A self-consistent study of the earth's radiation belts, *J. Geophys. Res.*, *72*, 4351, 1967.

Burton, R. K., R. L. McPherron, and C. T. Russell, An empirical relationship between interplanetary conditions and *Dst*, *J. Geophys. Res.*, *80*, 4204, 1975.

Cade, W. B., III, J. J. Sojka, and L. Zhu, A correlative comparison of the ring current and auroral electrojets using geomagnetic indices, *J. Geophys. Res.*, *100*, 97, 1995.

Carovillano, R. L., and G. L. Siscoe, Energy and momentum theorems in magnetospheric processes, *Rev. Geophys.*, *11*, 289, 1973.

Chen, C.-K., R. A. Wolf, M. Harel, and J. L. Karty, Theoretical magnetograms based on quantitative simulation of a magnetospheric substorm, *J. Geophys. Res.*, *87*, 6137, 1982.

Chen, M. W., L. R. Lyons, and M. Schulz, Simulations of phase space distributions of storm time proton ring current, *J. Geophys. Res.*, *99*, 5745, 1994.

Chen, M. W., L. R. Lyons, and M. Schulz, Stormtime ring-current formation: A comparison between single-and double-dip model storms

with similar transport characteristics, *J. Geophys. Res.*, *105*, 27,755, 2000.

Chiu, Y. T., and M. Schulz, Self-consistent particle and parallel electrostatic field distributions in the magnetospheric-ionospheric auroral region, *J. Geophys. Res.*, *83*, 629, 1978.

Crooker, N. U., and G. L. Siscoe, Model geomagnetic disturbance from asymmetric ring current particles, *J. Geophys. Res.*, *79*, 589, 1974.

Crooker, N. U., and G. L. Siscoe, Birkeland currents as the cause of the low-latitude asymmetric disturbance field, *J. Geophys. Res.*, *86*, 11,201, 1981.

Davis, T. N., and R. Parthasarathy, The relationship between polar magnetic activity Dp and growth of the geomagnetic ring current, *J. Geophys. Res.*, *72*, 5825, 1967.

Dessler, A. J., and E. N. Parker, Hydromagnetic theory of geomagnetic storms, *J. Geophys. Res.*, *64*, 2239, 1959.

Ebihara, Y., and M. Ejiri, Modeling of solar wind control of the ring current buildup: A case study of the magnetic storms in April 1997, *Geophys. Res. Lett.*, *25*, 3751, 1998.

Ebihara, Y., and M. Ejiri, Simulation study on fundamental properties of the storm-time ring current, *J. Geophys. Res.*, *105*, 15,843, 2000.

Ebihara, Y., and M. Ejiri, Reply to comment on "Simulation study on fundamental properties of the storm-time ring current" by V. M. Vasyliunas, *J. Geophys. Res.*, *106*, 6323, 2001.

Fok, M.-C., T. E. Moore, and D. C. Delcourt, Modeling of inner plasma sheet and ring current during substorms, *J. Geophys. Res.*, *104*, 14,557, 1999.

Friedrich, E., G. Rostoker, and M. G. Connors, Influence of the substorm current wedge on the *Dst* index, *J. Geophys. Res.*, *104*, 4567, 1999.

Grafe, A., Are our ideas about *Dst* correct?, *Ann. Geophys.*, *17*, 1–10, 1999.

Grafe, A., and Y. I. Feldstein, About the relationship between auroral electrojets and ring currents, *Ann. Geophys.*, *18*, 874, 2000.

Greenspan, M. E., and D. C. Hamilton, A test of the Dessler-Parker-Sckopke relation during magnetic storms, *J. Geophys. Res.*, *105*, 5419, 2000.

Hoffman, R. A., and P. A. Bracken, Higher-order ring currents and particle energy storage in the magnetosphere, *J. Geophys. Res.*, *72*, 6039, 1967.

Jordanova, V. K., C. J. Farrugia, J. M. Quinn, R. M. Thorne, K. W. Ogilvie, R. P. Lepping, G. Lu, A. J. Lazarus, M. F. Thomsen, and R. D. Belian, Effects of wave-particle interactions on ring current evolution for January 10–11, 1997: Initial results, *Geophys. Res. Lett.*, *25*, 2971, 1998.

Jordanova, V. K., L. M. Kistler, C. J. Farrugia, and R. B. Torbert, Effects of inner magnetospheric convection on ring current dynamics: March 10–12, 1998, *J. Geophys. Res.*, *106*, 29,705, 2001.

Jorgensen, A. M., H. E. Spence, M. G. Henderson, G. D. Reeves, M. Sugiura, and T. Kamei, Global energetic neutral atom (ENA) measurements and their association with the *Dst* index, *Geophys. Res. Lett.*, *24*, 3173, 1997.

Khazanov, G. V., M. W. Liemohn, and T. E. Moore, Photoelectron effects on the self-consistent potential in the collisionless polar wind, *J. Geophys. Res.*, *102*, 7509, 1997.

Khazanov, G. V., M. W. Liemohn, T. E. Moore, and E. N. Krivorutsky, Generalized kinetic description of steady-state interactions of a plasma with an arbitrary potential energy structure, *J. Geophys. Res.*, *103*, 6871, 1998.

Knight, S., Parallel electric fields, *Planet. Space Sci.*, *21*, 741, 1973.

Kozyra, J. U., V. K. Jordanova, J. E. Borovsky, M. F. Thomsen, D. J. Knipp, D. S. Evans, D. J. McComas, and T. E. Cayton, Effects of a high-density plasma sheet on ring current development during the November 2–6, 1993, magnetic storm, *J. Geophys. Res.*, *103*, 26,285, 1998.

Kozyra, J. U., M. W. Liemohn, C. R. Clauer, A. J. Ridley, M. F. Thomsen, J. E. Borovsky, J. L. Roeder, V. K. Jordanova, and W. D. Gonzalez, Multistep *Dst* development and ring current composition changes during the 4–6 June 1991 magnetic storm, *J. Geophys. Res.*, *107*(A8), 1224, doi:10.1029/2001JA000023, 2002.

Lackner, K., Deformation of a magnetic dipole field by trapped particles, *J. Geophys. Res.*, *75*, 3180, 1970.

Lemaire, J., and M. Scherer, Plasma sheet particle precipitation: A kinetic model, *Planet. Space Sci.*, *21*, 281, 1973.

Lemaire, J., and M. Scherer, Ionosphere-plasmasheet field-aligned currents and parallel electric fields, *Planet. Space Sci.*, *22*, 21,485, 1974.

Liemohn, M. W., and G. V. Khazanov, Collisionless plasma modeling in an arbitrary potential energy distribution, *Phys. Plasmas*, *6*, 585, 1998.

Liemohn, M. W., and J. U. Kozyra, Assessing the importance of convective and inductive electric fields in forming the stormtime ring current, in *Sixth International Conference on Substorms*, edited by R. W. Winglee, p. 456, Univ. of Wash., Seattle, Wash., 2002.

Liemohn, M. W., J. U. Kozyra, V. K. Jordanova, G. V. Khazanov, M. F. Thomsen, and T. E. Cayton, Analysis of early phase ring current recovery

mechanisms during geomagnetic storms, *Geophys. Res. Lett.*, *25*, 2845, 1999.

Liemohn, M. W., J. U. Kozyra, M. F. Thomsen, J. L. Roeder, G. Lu, J. E. Borovsky, and T. E. Cayton, Dominant role of the asymmetric ring current in producing the stormtime *Dst**, *J. Geophys. Res.*, *106*, 10,883, 2001a.

Liemohn, M. W., J. U. Kozyra, C. R. Clauer, and A. J. Ridley, Computational analysis of the near-Earth magnetospheric current system, *J. Geophys. Res.*, *106*, 29,531, 2001b.

Lui, A. T. Y., and D. C. Hamilton, Radial profiles of quiet time magnetospheric parameters, *J. Geophys. Res.*, *97*, 19,325, 1992.

Lui, A. T. Y., R. W. McEntire, and S. M. Krimigis, Evolution of the ring current during two geomagnetic storms, *J. Geophys. Res.*, *92*, 7459, 1987.

Lui, A. T. Y., H. E. Spence, and D. P. Stern, Empirical modeling of the quiet time nightside magnetosphere, *J. Geophys. Res.*, *99*, 151, 1994.

Maguire, J. J., and R. L. Carovillano, Effect of the interplanetary field on energy of geomagnetic disturbances, *J. Geophys. Res.*, *73*, 3395, 1968.

McPherron, R. L., The role of substorms in the generation of magnetic storms, in *Magnetic Storms, Geophys. Monogr. Ser.*, vol. 98, edited by B. T. Tsurutani et al., pp. 131, AGU, Washington, D. C., 1997.

Miller, R. H., and G. V. Khazanov, Self-consistent electrostatic potential due to trapped plasma in the magnetosphere, *Geophys. Res. Lett.*, *20*, 1331, 1993.

Munsami, V., Determination of the effects of substorms on the storm-time ring current using neural networks, *J. Geophys. Res.*, *105*, 27,833, 2000.

O'Brien, T. P., and R. L. McPherron, An empirical phase space analysis of ring current dynamics: Solar wind control of injection and decay, *J. Geophys. Res.*, *105*, 7707, 2000.

Ohtani, S., M. Nosé, G. Rostoker, H. Singer, A. T. Y. Lui, and M. Nakamura, Storm-substorm relationship: Contribution of the tail current to *Dst*, *J. Geophys. Res.*, *106*, 21,199, 2001.

Olbert, S., G. L. Siscoe, and V. M. Vasyliunas, A simple derivation of the Dessler-Parker-Sckopke relation, *J. Geophys. Res.*, *73*, 1115, 1968.

Parker, E. N., Newtonian development of the dynamical properties of ionized gases of low density, *Phys. Rev.*, *107*, 924, 1957.

Parker, E. N., and H. A. Stewart, Nonlinear inflation of a magnetic dipole, *J. Geophys. Res*, *72*, 5287, 1967.

Pulkkinen, T. I., N. Y. Ganushkina, D. N. Baker, N. E. Turner, J. F. Fennell, J. Roeder, T. A. Fritz, M. Grande, B. Kellett, and G. Kettmann, Ring current ion composition during solar minimum and rising solar activity: Polar/CAMMICE/MICS results, *J. Geophys. Res.*, *106*, 19,131, 2001.

Roble, R. G., and E. C. Ridley, An auroral model for the NCAR thermospheric general circulation model (TGCM), *Ann. Geophys., Ser. A*, *5*, 369, 1987.

Roeder, J. L., J. F. Fennell, M. W. Chen, M. Grande, S. Livi, and M. Schulz, CRRES observations of stormtime ring current ion composition, in *Workshop on the Earth's Trapped Particle Environment, AIP Conf. Proc.*, vol. 383, edited by G. D. Reeves, p. 131, Am. Inst. of Phys., Woodbury, N. Y., 1996.

Sckopke, N., A general relation between the energy of trapped particles and the disturbance field near the Earth, *J. Geophys. Res.*, *71*, 3125, 1966.

Sheldon, R. B., and D. C. Hamilton, Ion transport and loss in the Earth's quiet ring current: 1. Data and standard model, *J. Geophys. Res.*, *98*, 13,491, 1993.

Siscoe, G. L., The virial theorem applied to magnetospheric dynamics, *J. Geophys. Res.*, *75*, 5340, 1970.

Siscoe, G. L., and N. U. Crooker, On the partial ring current contribution to *Dst*, *J. Geophys. Res.*, *79*, 1110, 1974.

Siscoe, G. L., and H. E. Petschek, On storm weakening during substorm expansion phase, *Ann. Geophys.*, *15*, 211, 1997.

Sozou, C., and D. W. Windle, A self-consistent ring current in the earth's dipole field, *Planet. Space Sci.*, *17*, 375, 1969a.

Sozou, C., and D. W. Windle, Non-linear symmetric inflation of a magnetic dipole, *Planet. Space Sci.*, *17*, 999, 1969b.

Stasiewicz, K., The influence of a turbulent region on the flux of auroral electrons, *Planet. Space Sci.*, *6*, 591, 1985.

Su, Y.-J., J. L. Horwitz, G. R. Wilson, P. G. Richards, D. G. Brown, and C. W. Ho, Self-consistent simulation of the photoelectron-driven polar wind from 120 km to 9 R_E altitude, *J. Geophys. Res.*, *103*, 2279, 1998.

Turner, N. E., D. N. Baker, T. I. Pulkkinen, and R. L. McPherron, Evaluation of the tail current contribution to *Dst*, *J. Geophys. Res.*, *105*, 5431, 2000.

Turner, N. E., D. N. Baker, T. I. Pulkinnen, J. L. Roeder, J. F. Fennell, and V. K. Jordanova, Energy content in the stormtime ring current, *J. Geophys. Res.*, *106*, 19,149, 2001.

Vasyliunas, V. M., Mathematical models of magnetospheric convection and its coupling to the ionosphere, in *Particles and Fields in the Magnetosphere*, edited by B. M. McCormac, p. 60, D. Riedel, Norwell, Mass., 1970.

Vasyliunas, V. M., A note on current closure, *J. Geophys. Res.*, *104*, 25,143, 1999.

Vasyliunas, V. M., Comment on "Simulation study on fundamental properties of the storm-time ring current" by Y. Ebihara and M. Ejiri, *J. Geophys. Res.*, *106*, 6321, 2001.

Whipple, E. C., The signature of parallel electric fields in a collisionless plasma, *J. Geophys. Res.*, *82*, 1525, 1977.

Wilson, G. R., G. V. Khazanov, and J. L. Horwitz, Achieving zero current for polar wind outflow on open flux tubes subjected to large photoelectron fluxes, *Geophys. Res. Lett.*, *24*, 1183, 1997.

Wolf, R. A., J. W. Freeman Jr., B. A. Hausman, R. W. Spiro, R. V. Hilmer, and R. L. Lambour, Modeling convection effects in magnetic storms, in *Magnetic Storms, Geophys. Monogr. Ser.*, vol. 98, edited by B. T. Tsurutani et al., p. 161, AGU, Washington, D. C., 1997.

―――――――――――

M. W. Liemohn, Space Physics Research Laboratory, University of Michigan, Ann Arbor, MI 48176, USA. (liemohn@umich.edu)